Journal of Geophysical Research: Space Physics

RESEARCH ARTICLE

Key Points:
- Jupiter's nightside auroral ionosphere is similar to the dayside
- Sub-auroral emission is concentrated close to the aurora, at eastward longitudes T
- This emission is best explained by sub-rotating winds flowing from the aurora

Cassini VIMS observations of H$_3^+$ emission on the nightside of Jupiter

Tom S. Stallard[1], Henrik Melin[1], Steve Miller[2], Sarah V. Badman[3], Kevin H. Baines[4], Robert H. Brown[5], James S. D. Blake[1], James O'Donoghue[6], Rosie E. Johnson[1], Bethany Bools[1], Nathan M. Pilkington[2], Oliver T.L. East[1], and Mark Fletcher[1]

[1]Department of Physics and Astronomy, University of Leicester, Leicester, UK, [2]Department of Physics and Astronomy, University College London, London, UK, [3]Department of Physics, Lancaster University, Lancaster, UK, [4]SSEC, University of Wisconsin-Madison, Madison, Wisconsin, USA, [5]Lunar and Planetary Laboratory and Steward Observatory, University of Arizona, Tucson, Arizona, USA, [6]Center for Space Physics, Boston University, Boston, MA, USA

Abstract We present the first detailed analysis of H$_3^+$ nightside emission from Jupiter, using Visual and Infrared Mapping Spectrometer (VIMS) data from the Cassini flyby in 2000–2001, producing the first Jovian maps of nightside H$_3^+$ emission, temperature, and column density. Using these, we identify and characterize regions of H$_3^+$ nightside emission, compared against past observations of H$_3^+$ emission on the dayside. We focus our investigation on the region previously described as "mid-to-low latitude emission," the source for which has been controversial. We find that the brightest of this emission is generated at Jovigraphic latitudes similar to the most equatorward extent of the main auroral emission but concentrated at longitudes eastward of this emission. The emission is produced by enhanced H$_3^+$ density, with temperatures dropping away in this region. This emission has a loose association with the predicted location of diffuse aurora produced by pitch angle scattering in the north, but not in the south. This emission also lays in the path of subrotating winds flowing from the aurora, suggesting a transport origin. Some differences are seen between dayside and nightside subauroral emissions, with dayside emission extending more equatorward, perhaps caused by the lack of sunlight ionization on the nightside, and unmeasured changes in temperature. Ionospheric temperatures are hotter in the polar region (~1100–1500 K), dropping away toward the equator (as low as 750 K), broadly similar to values on the dayside, highlighting the dominance of auroral effects in the polar region. No equatorial emission is observed, suggesting that very little particle precipitation occurs away from the polar regions.

1. Introduction

Our understanding of Jupiter's ionosphere and upper atmosphere has been significantly enhanced in the past two decades through the use of the ionic molecule H$_3^+$ as an atmospheric probe. First detected by *Drossart et al.* [1989], this molecule has a number of unique characteristics that make it particularly useful. It is readily produced in the upper atmosphere but quickly destroyed in the lower atmosphere [*Miller et al.*, 2006]. H$_3^+$ is quickly thermalized within the surrounding neutral atmosphere, allowing its presence to be used as a measure of the atmospheric temperature [e.g., *Lam et al.*, 1997; *Stallard et al.*, 2002]. As an ion it provides an indication of currents running through the ionosphere [*Stallard et al.*, 2001]. It also happens to coincidentally emit strongly at wavelengths where light is strongly absorbed by methane in the lower atmosphere of Jupiter. This means that H$_3^+$ can be observed as a bright glow above a dark underlying planetary disk.

H$_3^+$ is created by a number of processes in the ionosphere of Jupiter. It is most strongly generated in polar regions by currents that flow from the surrounding magnetosphere down along magnetic field lines, closing through the ionosphere. These currents accelerate energetic electrons into the planet, driving ionization of molecular hydrogen:

$$H_2 + e^* \rightarrow H_2^+ + e + e$$
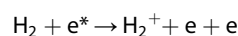
The resultant H$_2^+$ almost instantaneously reacts with more H$_2$ to produce H$_3^+$:

$$H_2^+ + H_2 \rightarrow H_3^+ + H$$
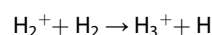
Although auroral H$_3^+$ dominates in the polar auroral regions, additional H$_3^+$ is produced at all latitudes, largely through two other processes, both of which produce H$_2^+$, which is similarly converted into H$_3^+$.

First is through ionization produced by solar extreme ultraviolet (EUV), resulting in a uniform ionization across the sunlit disk of the planet:

$$H_2 + hn \rightarrow H_2^+ + e$$
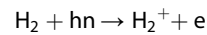
Secondly, H_3^+ is created through the reaction between protons and energetic molecular hydrogen, created by the same ionization processes as H_2^+ but typically surviving for much longer within the ionosphere:

$$H^+ + H_2(v \geq 4) \rightarrow H_3^+ + hn$$
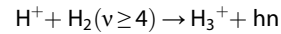
Once H_3^+ is created in the ionosphere, it is destroyed by two significant processes. If H_3^+ is generated below Jupiter's homopause, in the presence of any molecule other than hydrogen or helium, it quickly protonates those molecules, removing H_3^+ from the ionosphere:

$$H_3^+ + X \rightarrow HX^+ + H_2$$
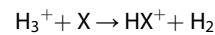
However, above the homopause, where only H and He reside, such reactions cannot take place. As a result, the lifetime of the H_3^+ molecule is directly controlled by dissociative recombination:

$$H_3^+ + e \rightarrow H_2 + H$$
$$\rightarrow H + H + H$$
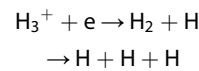
The rate at which this reaction occurs is controlled by the electron density in Jupiter's atmosphere. The recombination rate has been modeled as ~10–15 min at the altitude of Jupiter's H_3^+ emission peak [*Achilleos et al.*, 1998]. While this is long enough for the H_3^+ to interact within the surrounding thermosphere, it essentially means that most H_3^+ remains close to the location of the original ionization of hydrogen, so that the H_3^+ column density can be used as a probe of the ionization processes within Jupiter's ionosphere. However, H^+ has a much longer timescale of recombination. While this is poorly constrained, recent observations (H. Melin, private communication, 2015) suggest that the H^+ lifetime is ~2 h in Jupiter's equatorial region. This may allow the production of H_3^+ further away from its originating ionization source, due to the transport of H^+ before its reaction with energetic molecular hydrogen.

The currents that produce auroral H_3^+ emission are dominated by those that link the ionosphere with the middle magnetosphere, where a plasmadisk that is drifting away from the planet is accelerated through a j×B restoring force and is thus forced to corotate with the planet by the magnetic field. At a distance of 20–30 R_J, the force required to maintain this corotation becomes larger than the force the weakening magnetic field can generate in the ions, resulting in a breakdown in corotation [*Cowley and Bunce*, 2001]. This breakdown drives a field-aligned current into the ionosphere and results in both powerful aurora produced by electron precipitation and large-scale ion winds in the ionosphere. In addition to this main auroral emission, there are also a number of emission spots produced at the magnetic footprints of the Galilean moons. The Io spot is also followed by a tail of emission that extends more than halfway around the planet [*Grodent et al.*, 2003a].

Although the broad-scale shape of Jupiter's magnetic field can be approximated by an offset tilted dipole, the northern auroral region is significantly distorted by a magnetic anomaly that can be characterized by a weakening of the surface magnetic field in the local region and by an added localized tilted dipole field, rotating with the planet at a depth of 0.245 R_J below the surface [*Grodent et al.*, 2008]. As such, while the southern auroral oval is largely circular, the northern auroral morphology is more complicated, with the auroral region having a shape reminisent of a kidney bean. The auroral "ovals" are roughly centered on the magnetic poles in each hemisphere, which are displaced from the planet's rotation axis.

Poleward of the main auroral region, there are also regions that are controlled by the solar wind, characterized by significant ion winds [*Stallard et al.*, 2003] and by short-term sporadic "swirl" emission [*Grodent et al.*, 2003b].

Although emission from Jupiter's main auroral features is well understood, the H_3^+ emissions seen equatorward of the Io spot and tail are far less well explained. This emission, described as "mid-to-low latitude" emission, was first detected by *Lam et al.* [1997]. *Miller et al.* [1997] made a more detailed analysis of this region and showed that emission levels are strongly dependent upon latitude and longitude, and the existence of H_3^+ at these latitudes is likely to be explained only by either transport from the auroral regions or particle precipitation from the inner magnetosphere.

Rego et al. [2000] made a more detailed analysis of sources of H_3^+ emission along the dayside rotational axis using a multi-emission-component model. This showed that the mid-to-low-latitude emission intensity varies between 1% and 40% of the peak auroral emission intensity in the north and between 2% and 16% in the south. Because of the relatively large region of the planet covered by this emission in comparison with the polar-bound aurora, the total auroral emission power of this mid-to-low latitude component is approximately half that of the auroral emission.

Morioka et al. [2004] showed that the extent to which this mid-to-low latitude emission covers the planet varies in proportion to the overall Jovian auroral power, which *Melin et al.* [2006] has shown to typically vary over periods of several days. This was used to suggest that the mid-to-low latitude emission is driven by precipitation from the inner magnetosphere and that there is an intrinsic link between the particle precipitation rates in the inner and middle magnetosphere, feeding the mid-to-low latitude and main oval emissions, respectively.

Subauroral emission is also seen at other wavelengths. Measurements of the Jovian UV dayglow suggest that photoelectron excitation cannot entirely account for the observed electron-excited H_2 emission and that this emission is dominated by precipitating radiation belt electrons [*Feldman et al.*, 1993]. The intensity of subauroral X-ray emissions was shown to be anticorrelated with the local magnetic field strength at different longitudes, suggesting the emissions were driven by particle precipitation [*Waite et al.*, 1997; *Gladstone et al.*, 1998].

Abel and Thorne [2003] modeled scattering of particles into the subauroral atmosphere resulting from asymmetries in the magnetic field (using the VIP-4 magnetic field model), with the particle precipitation flux—and thus the relative H_3^+ emission—strongly anticorrelated with magnetic field strength. The weaker overall magnetic field strength in the southern hemisphere predicted slightly increased emission there; at Jovimagnetic latitudes mapping to a distance from the planet of 1.5 R_J, the overall southern flux would be 50% brighter than the overall northern flux, but for Jovimagnetic latitudes mapping to 4 R_J, the overall flux should be similar in the two hemispheres. However, magnetic field strengths also vary significantly as a function of magnetic longitude for any particular magnetic latitude. This variation is far stronger in the north, and so the northern emission intensity should be highly dependent upon longitude, with H_3^+ emission varying by orders of magnitude as the magnetic field strength changes. This model suggested that the observed low-latitude H_3^+ emissions in the northern hemisphere, measured by *Miller et al.* [1997], could be explained at least in part by this process but not those in the southern hemisphere.

The temperature and energy balance in Jupiter's auroral region have been studied in some detail [e.g., *Lam et al.*, 1997; *Stallard et al.*, 2002; *Raynaud et al.*, 2004; *Lystrup et al.*, 2008], and all show high temperatures within the auroral region, varying between 900 K and 1400 K, with temperature often correlated with emission brightness. *Melin et al.* [2006] modeled the temperatures within one particular auroral event and showed that these were largely driven by Joule heating associated with the currents flowing through the ionosphere, rather than directly with the auroral precipitation itself.

Lam et al. [1997] remains the only currently published measurements of Jovian subauroral temperature. This study showed temperatures decreasing with latitude, as low as 700 K at 50° latitude, before rising again to ~900 K at the equator. However, the fit for these temperature measurements was significantly restricted by an apparent anticorrelation between temperature and column density and so may not accurately describe the thermal conditions away from the auroral regions.

All the studies described above relied on observations made by ground-based telescopes and were therefore restricted to studying Jupiter's dayside emissions. Nightside observations of Jupiter's aurora have been made in the past, for example, in the visible [*Vasavada et al.*, 1999] and UV [*Gladstone et al.*, 2007], but these have been focused on very localized regions of the main auroral emission. In this study, we analyze data taken during the Cassini flyby in order to measure H_3^+ emission from Jupiter as a function of latitude, allowing the first measurements of H_3^+ intensity on Jupiter's nightside, as well as the first long-term temporally averaged temperatures within Jupiter's auroral region.

2. Observations

The Cassini spacecraft passed Jupiter on its way to Saturn, with Cassini reaching closest approach on the dawn flank of the planet, close to the equatorial plane, on 30 December 2000, at a distance of 136 R_J (1 R_J = 71,492 km). The trajectory of Cassini over this interval is shown in Figure 1 in Jupiter Solar Equatorial (JSE) coordinates, where
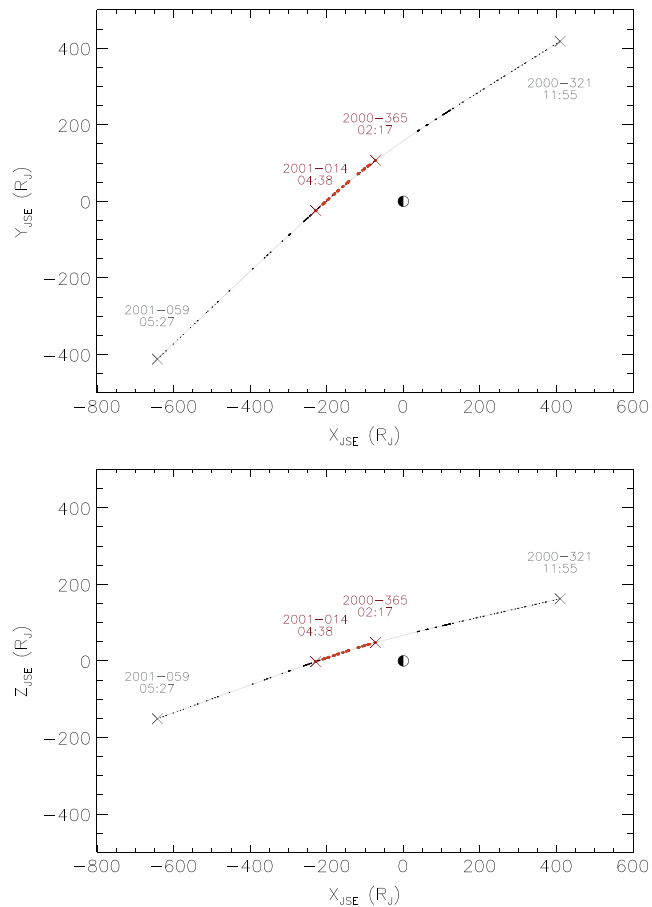
Figure 1. The location of Cassini at the times when VIMS took images of Jupiter, projected onto the *X-Y* and *X-Z* planes, in distance from Jupiter. The path of Cassini during the flyby is marked as a grey line, with all the images taken shown as black dots along this line. The images used in this study are highlighted as bold red points. Jupiter is not to scale. *X*, *Y*, and *Z* are in Jupiter Solar Equatorial (JSE) coordinates, and the start and end times and dates are provided for all the Jupiter observations (black) and the observations used in this study (red).

x points from Jupiter to the Sun, *y* is perpendicular to the rotation axis pointing toward dusk, and *z* points parallel to the rotational axis toward Joviographic north.

During this flyby the Visual and Infrared Mapping Spectrometer (VIMS) [*Brown et al.*, 2003] observed Jupiter both as a functional test of the instrument and in order to specifically provide scientific observations of the Jovian system. The VIMS instrument began taking observations of Jupiter on 16 November 2000 and continued until 28 February 2001, providing a total of 1915 images.

Even at closest approach, VIMS was able to easily fit the entire planetary disk into its 32 mrad × 32 mrad field of view, such that the planet was contained within at most 24 × 24 pixels (where 1 pixel is 0.5 mrad × 0.5 mrad in size). This limited spatial resolution greatly restricts the amount of detailed science that can be performed with individual images. However, our study combines these individual images into a longitude-latitude map of H_3^+ emission measured on the nightside of the planet, as the planet rotated under the instrument field of view, which can then be combined into latitudinal profiles of both emission and temperature. While measurements of emission structure and temperature require the same broad-scale analysis, the specific requirements of each (spatial resolution and spectral accuracy, respectively) require some differences in the way data is combined.
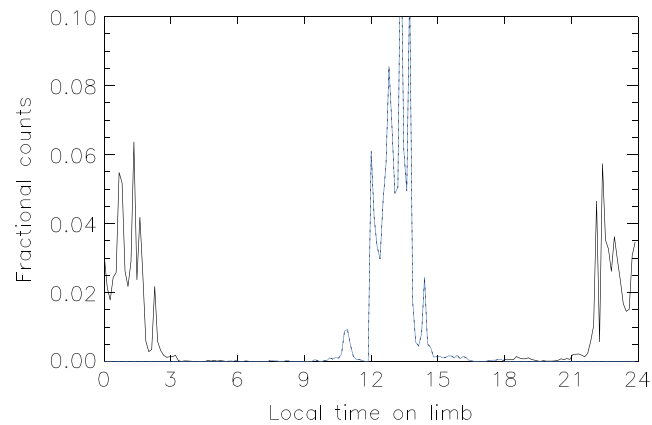
As such, only images taken under specific conditions were included in this study. Before more detailed processing, all images were assessed using the following limitations:

1. The image size taken was more than 16 pixels across; our technique requires a measure of the background light away from the planet, and small images do not provide enough information to be useful.
2. The image exposure time was greater than 15 ms per pixel; although shorter timescales could be used, they were removed to improve processing time, as they would contribute relatively little when the majority of images had a 640 ms integration time.
3. The image was taken from within 17 million km (238 R_J) of the planet; this empirically defined distance limitation avoids images with too low a spatial resolution on Jupiter.
4. The image contains at least some of Jupiter's disk; several images were taken of calibration stars and other objects.
5. Cassini was further from the Sun than Jupiter; we found empirically that observations taken sunward of Jupiter included significant reflected sunlight, even on the nightside limb, as the sunlit crescent approached too close across the planetary disk seen by Cassini.

Figure 2. A histogram, with 2° bins, showing the fraction of local times observed within this study, on a pixel-by-pixel basis, for the nightside (solid black line) and the dayside (dotted blue line), where the total fractional counts for each equate to 1.

These limitations result in a remaining 277 images. The exact locations of where these two reduced sets of VIMS images were taken are also shown in Figure 1 by the larger red dots. These images cover a range of local times on the planetary limb, as shown in Figure 2, but are concentrated 3 h duskward of noon on the dayside and at 3 h either side of midnight on the nightside.

A variety of different integration times were used during the flyby, ranging between 20 ms and 640 ms per pixel. While this could represent a total image integration time of up to 40 min, since we are processing these images on a pixel-by-pixel basis, we can ignore the effect of spatial smearing caused by planetary rotation. In addition, two instrument modes were used in these observations, normal and high spatial resolution, in which the *x* direction of the spectrometer scans in 0.5 pixel steps—both these data types are included in this study and again, on a pixel-by-pixel basis, both observing types produce effectively identical outputs.

3. Data Analysis

The VIMS instrument covers the wavelength range 0.3–5.2 μm in 352 spectral channels, divided into a visual and infrared wavelength component. This study uses a selection of wavelength bins from the 256 available within the infrared range of VIMS (see *Brown et al.* [2003] for details of the VIMS instrument configuration). These light in each bin are measured after having been split using a diffraction grating, so that each bins measures a wavelength range that approximates to a Gaussian filter centered on a particular wavelength, with an approximate spectral resolution for each bin of $\lambda/\Delta\lambda$ ~300. As a result, so it can often be difficult to resolve specific sources of measured intensity in individual bins. However, while reflected sunlight, H_3^+ emission, and thermal emission all overlap in wavelength range to some extent, there are wavelength regions between 2 and 5 μm where each of the three sources dominates the Jovian spectra.
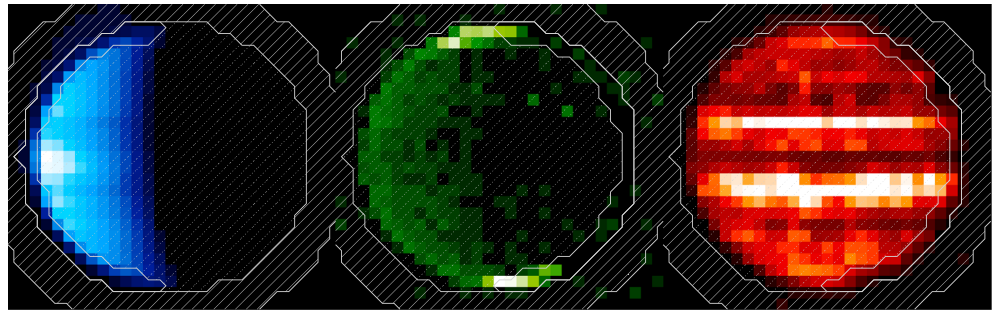
Figure 3 shows an example observation taken on 7 January 2001 at 20:11, from a radial distance of 172.2 R_J, at three selected wavelengths. Solar emission dominates the image at 2.698 μm (bin 110) (Figure 3, left). At 3.417 μm (bin 153), both solar reflection and thermal emission are weaker, while two relatively bright fundamental lines of H_3^+, R(3,0$^-$), and R(3,1$^+$) allow a strong auroral emission to be seen in the polar regions (Figure 3, middle). The thermal component in the image at 5.043 μm (bin 250) grows stronger at longer wavelengths and completely dominates over reflected sunlight shown (Figure 3, right).

3.1. Individual Pixel Intensities

VIMS spectral images are constructed using two mirrors that sweep across the area of the image, scanning horizontally and then vertically. As such, the total image can take an extended period to produce, but every wavelength bin is simultaneously filled for each individual pixel. In this study, we will use each pixel as its own separate measurement, using the pointing geometry of Cassini and the VIMS boresight derived from NASA's Navigation and Ancillary Information Facility (NAIF) [*Acton*, 1996], in order to calculate the planetary positioning information for each pixel. From the pointing geometry, we define a straight line in the plane of the field of view that runs from the center of the planet, through the center or corner of the pixel, and onto the limb of the planet. Using this, it is possible to calculate for each pixel the corresponding latitude, longitude, and local time on the limb of the planet, as well as the distance from the limb, assuming that the planetary values are contributed at the tangent point of the line-of-sight, as shown in Figure 4.

Figure 3. An example set of a typical VIMS image of Jupiter taken on 7 January 2001 from a position of −169.7, 29.4, and 18.2 R_J in the x, y, and z directions, respectively. The three panels show three wavelengths: (left) 2.70 μm (reflected sunlight), (middle) 3.42 μm (H_3^+ emission), and (right) 5.04 μm (thermal emission). Two regions are used in our study, the first a region within 5000 km of the limb, on the nightside of the planet, and indicated on the nightside in the outline drawn on Figures 3 (middle) and 3 (right). The second is the background at a distance >25,000 km from the limb, again indicated by an outline. Other regions are ignored and are shaded with oblique lines, solid off the planet, and dotted on the planet. The field of view here is 32×32 pixels, or $16\,\text{mrad} \times 16\,\text{mrad}$.

Using this geometric information it is then possible to define which pixels within each image will be included in our H_3^+ map, and so we preferentially chose those pixels where the H_3^+ signal is clearest:

1. H_3^+ is strongly limb brightened, so that along the edge of the planet, the measured H_3^+ signal is relatively much brighter than either the solar or thermal light, which typically weaken toward the limb. We have empirically chosen to use pixels whose center is within 5000 km of the limb of the planet, as this gathers a significant proportion of the limb-brightened H_3^+ emission and avoids regions too far from the limb.
2. Using only the nightside emission effectively removes nearly all the solar-reflected sunlight from the signal. For the thermal emission, as well as a subset of H_3^+ measurements, we use only pixels with a local time 6 h before or after midnight. When measuring the solar spectra and dayside H_3^+, we use the opposite of this, taking pixels with local time 6 h before or after noon.

The combination of these effects limits the data used to a relatively small number of pixels along the limb of the planet, on either the dayside or nightside, a region identified in Figure 3.

Since H_3^+ is at an altitude of ~400 km above the 1 bar level, and the line-of-sight path of H_3^+ is only blocked below this level, the ionosphere emits as a shell of emission, potentially resulting in a longitudinal/local time error of up to about ±7° at the equator and about ±12° in the auroral region. This error is reduced by the line-of-sight enhancement of H_3^+ (shown in Figure 13) focusing emission to a narrower range of longitudes. However, since Cassini is close to the equatorial plane of Jupiter, the error in latitude is minimized (see Figure 4).
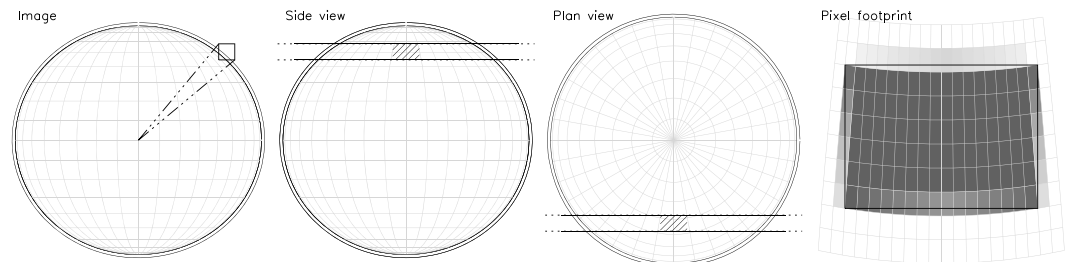
Figure 4. A cartoon showing how geometric information is measured within an image. The corners of each pixel are mapped back to the center of the planet (far left); this distance provides the rayheight for each corner; where this straight line crosses the limb provides specific information about the latitude and longitude on the limb. The path of the line-of-sight passes the planet (side view, left) such that the available longitude range above the 1 bar level is ~ ±7° longitude. This results in almost no variation in latitude (plan view, right), as the line-of-sight path covers lines of equal latitude as it passes this region. Once the latitude and longitude range of the pixel is measured, the footprint of the pixel is mapped onto a latitude-longitude grid (pixel footprint, far right), a fractional value for each grid position is calculated, and the intensity and integration time is factored by this fraction within each grid position. This process is then repeated across each pixel, in each image, with the fractional intensity and integration time totalled within each grid position.
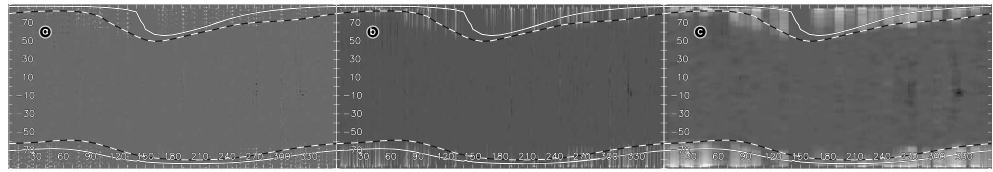
Figure 5. The latitude-longitude map of intensity from the VIMS bin centered on 3.530 μm. (a) Individual pixel intensities are mapped against specific points in latitude and west longitude (SIII). (b) Each pixel is mapped to the fractional range of latitudes covered by that pixel. (c) Both the fractional range of latitudes and an estimated ±5° of longitude are mapped for each pixel. Also shown are the 30 R$_J$ (solid line) and 5.9 R$_J$ (dashed line) magnetic latitudes [*Grodent et al.*, 2008].

We also require a measurement of the background signal in the array. Past analysis of VIMS data [e.g., *Stallard et al.*, 2008] has shown that VIMS images often have significant variations in the background level, but that this variation is typically constant for any one particular image row. As such, we can calculate a background for a specific pixel by taking the mean value for pixels within the same image row that are significantly distant from the planet (we assume a distance greater than 25,000 km from the limb is suitably distant to avoid planetary contamination). This second region is also shown in Figure 3, outside the diagonally shaded region. Thus, for each pixel, we measure the brightness in each individual wavelength bin and subtract from this the mean background brightness for that particular bin, calculated from the background pixels with the same row as the pixel in question.

Once the background is subtracted, a final check on the pixel bin intensity is made, to ensure the value is not far outside the range of expected values. This check removes any bad pixels or intensities caused by cosmic rays or other nonplanetary sources. Pixel bin data are excluded if the measured bin intensity is below -0.5, a value far too low to be real, or above 0.5, 1, 2, 8, or 1e4 μWm^{-2} μm^{-1} sr^{-1} in bins 1–180, 180–189, 191–199, 200–209, or 210+, respectively, where individual H$_3^+$ intensities peak around 0.1 μWm^{-2} μm^{-1} sr^{-1}. These values are increased for longer wavelengths, as thermal emission increases the range of reasonable values significantly.

3.2. Latitude-Longitude Maps

Having removed the background from a pixel, the intensity contained within the pixel is a measure of the mean intensity across latitude and longitude region covered by that pixel.

The length of each individual image is short enough that it acts as an effective snapshot of Jupiter at the time of observations. The measured intensity is an unweighted average of the spatially variable line-of-sight Jovian intensity on the limb of the planet. This in turn represents a slice of the H$_3^+$ ionosphere on and above the limb of the planet, enhanced by the line-of-sight effect. In calculating the range of latitudes and longitudes that map to that particular part of the limb, the pixel footprint can be defined by a latitude and longitude range. Using NAIF, we have calculated the positional information for pixels both above and below the planetary limb, and using these coordinates, we have mapped all the pixels within all the images on a map of latitude and longitude, shown in the left panel of Figure 5a. However, such a mapping ignores that a pixel actually covers a range of latitude and longitude ranges, and it is necessary to include this distribution for each pixel to properly map. The latitudinal range of a pixel is calculated by measuring the minimum and maximum extent of the limb latitudes covered by the pixel and then adding the fractional contribution within each latitudinal position to the map, as shown in Figure 5b; this has the effect of smoothing the intensities in the latitudinal direction. The longitudinal extent of each pixel is dominated by the range of longitudes measured in the line-of-sight column observed above the limb. Here we approximate this as a range of ±5° from the limb longitude, which is distributed uniformly over 10°, for simplicity. Combining these mappings for all images produces a series of final intensity maps, one for each bin, as shown in Figure 5c.

With data from multiple pixels and exposures being considered, some footprints must overlap. Averaging these mean specific intensities where their footprints overlap, by weighting them by their individual observation exposure times (normalized to the total exposure time of each observation), should improve the intensity estimate of the included mapped elements.
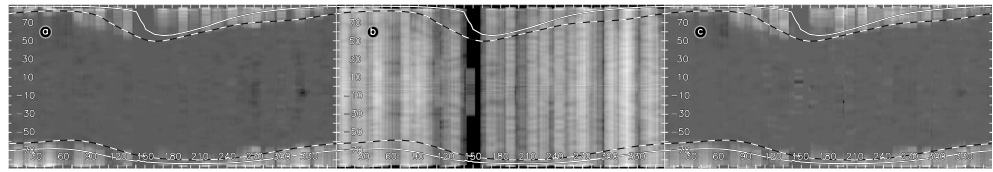
Figure 6. The scaled intensity in the VIMS bin centered on 3.530 μm. (a) Total intensity measured after each subpixel has been coadded, the same image as Figure 5c. (b) Total integration time, a combination of the fractional integration time from each pixel. (c) Mean intensity, produced from the total intensity divided by the integration time. Also shown are the 30 R_J (solid line) and 5.9 R_J (dashed line) magnetic latitudes [*Grodent et al.*, 2008].

To do this, we actually produce two sets of latitude-longitude bin maps for each bin of each image, one for the total bin intensity (which is shown in Figures 5c and 6a) and one for the fractional bin integration time (shown in Figure 6b). The fractional bin integration time provides a divisor to the total bin intensity that allows the mean intensity to be calculated; it is produced by factoring the integration time for a pixel against the fraction that a pixel contributes to each latitude and longitude, summed across all the pixels included in the measurement. In order to calculate the mean intensity map for each wavelength bin (shown in Figure 6c), the total bin intensity is divided by the fractional bin integration time map, resulting in an accurate measurement of mean intensity in $\mu Wm^{-2} \mu m^{-1} sr^{-1}$.

3.3. Spectral Correction

Using the above process, it is possible to produce a mean intensity map for every wavelength bin, using light from either the dayside or nightside limbs of the planet. However, within each individual wavelength bin, the light measured includes contributions from reflected sunlight and thermal emission, and so, in order to measure the pure H_3^+ emission, it is necessary to measure and remove these other sources of intensity. As was shown in Figure 3, reflected sunlight dominates at shorter wavelengths and thermal emission dominates at longer wavelengths. Figure 7 shows six intensity maps, with the top row
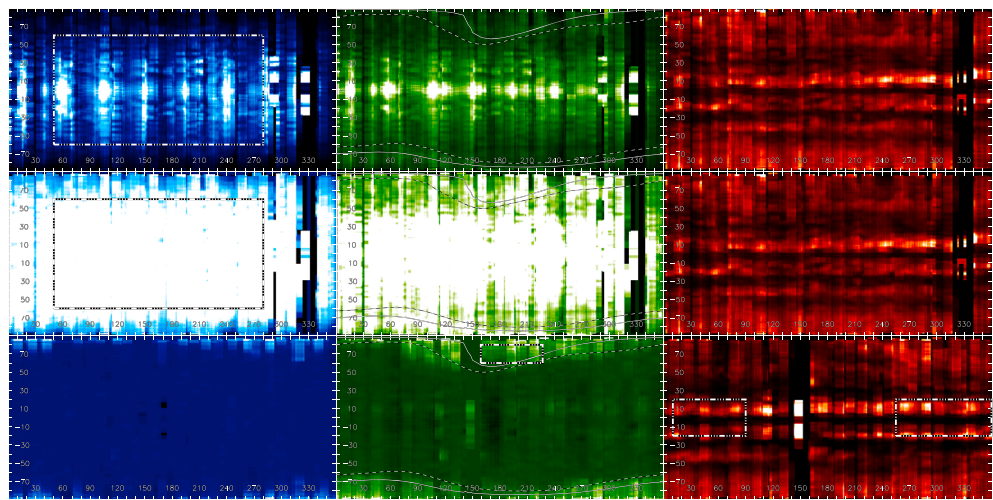
Figure 7. (top) Intensity maps of the dayside, (middle) dayside scaled to nightside brightness, and (bottom) nightside reflected sunlight, H_3^+ emission, and thermal emission. Maps are gridded in longitude in the *x* axis and latitude in the *y* axis (with a pixel representing 1° in each dimension). The sunlight component (left column; seen only in light extending over the poles from the dayside) is produced by the sum of bins between 2.632 and 2.868 μm. The thermal component (right column) is the sum of bins between 4.772 and 5.093 μm. The H_3^+ emission (middle column) is the sum of bins between 3.197 and 4.315 μm, with the scaled solar and thermal components removed. Each image is normalized and includes a power scaling to highlight lower level emission. Jovicentric latitude and longitude (SIII) are marked in steps of 10°. The regions used to produce the spectra shown in Figure 8 are also shown (as dash-triple dotted regions); in the top left and middle left panels for the reflected sunlight spectrum, in the bottom central panel for the H_3^+ spectrum, and in the bottom right panel for the thermal emission spectrum. Also shown in the central panels are the 30 R_J (solid line) and 5.9 R_J (dashed line) magnetic latitudes [*Grodent et al.*, 2008]. Also note that the nightside emission between 160 and 180°W_{III}, resulting in significant equatorial errors in both the H_3^+ and thermal emission in this region.
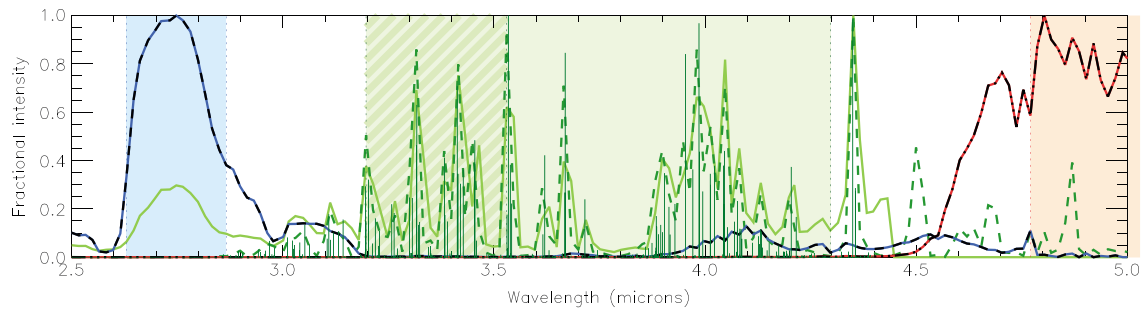
Figure 8. The normalized spectral components of light from Jupiter between 2 and 5 μm, produced by coadding light from all the images used in this study. Three dominant components are shown. Thermal emission (dash-triple dotted red line) from Jupiter's interior is dominant at wavelengths greater than ~4.3 μm; this spectrum is the light measured on the nightside limb of the planet at latitudes between 20°N and −20°S. Reflected sunlight (dark blue dashed line) dominates at short wavelengths; this was measured on the dayside limb of the planet at latitudes between 60°N and −60°S and has had the scaled thermal emission subtracted from it. H_3^+ emission (vertical lines for the H_3^+ emission lines at 900 K, dashed green for the modeled VIMS response to these lines, and bold green line for the H_3^+ emission observed at the resolution of VIMS) is brightest in the 3–4.5 μm region. Three wavelength regions are identified by shaded backgrounds (blue, green, and red, respectively) and represent the regions used to produce the maps shown in Figure 7. In addition, the green region includes a smaller wavelength range (angled darker green shading) that denotes a narrower region of H_3^+ emission used in sections 4 and 6.

showing the measured intensities on the dayside limb and the bottom row showing the nightside limb. These images represent the combined intensities from three wavelength ranges, the three columns in the figure, with sunlight-dominated wavelengths between 2.632 and 2.868 μm (combining bins 106 and 120, the left column shown in blue), thermal-dominated wavelengths between 4.772 and 5.093 μm (bins 234 and 253, the right column shown in red), and the wavelengths where H_3^+ emission is brightest between 3.197 and 4.315 μm (bins 140 and 207, the middle column shown in green). On the dayside, the region of H_3^+ emission is clearly dominated by reflected sunlight, with little evidence of H_3^+ emission. On the nightside the H_3^+ emission near the poles is clearly seen; though some reflected sunlight is also seen at the poles, leaking over from the dayside, and close to the equator, the intensity structure is dominated by thermal emission.

In order to produce maps of pure H_3^+ emission, we can use the maps of the nightside sunlight and thermal emission shown in Figure 7 to subtract the intensity caused by these sources from our data, but the extent to which each of these maps contributes to any particular wavelength bin varies significantly. As such, we need to produce a measure of how the relative brightness of sunlight and thermal emission vary with wavelength.

To do this, we have produced two normalized intensity spectra for reflected sunlight and thermal emission. We measure thermal emission using the combined intensity across all the images from pixels on the nightside limb at latitudes between 20°N and −20°S, and for selected longitudes; these regions are shown by the dotted line in Figure 7 (bottom right). This region is completely free of any sunlight contamination, has the peak thermal emission, and is the region where H_3^+ emission is weakest. As such, the resultant normalized spectra, shown as the dark red dashed line in Figure 8, are almost pure thermal emission from Jupiter. We measure the reflected sunlight spectrum in a similar way, using pixels on the dayside limb at latitudes between 60°N and −60°S, and for selected longitudes; these regions are shown by the dotted line in the Figure 7 (top left). While the solar emission strongly dominates over the H_3^+ emission in this region, the dayside light includes contributions from both sunlight and thermal emission within it. Thus, we remove thermal emission from this spectrum by subtracting the thermal spectra described above, normalized to the intensity measured from the dayside in the 4.772–5.093 μm wavelength range, where thermal emission again dominates. This leaves a normalized intensity spectrum that is dominated by reflected sunlight, shown as the dark blue dashed line in Figure 8.

In order to remove the effects of sunlight and thermal emission from the bin maps of latitude and longitude, we normalize each of the spectra in Figure 8 to the mean emission from the wavelength regions covered by the nightside sunlight and thermal maps that we will be subtracting; these regions are shown in Figure 8 as blue and red shaded regions. Then, on a bin-by-bin basis, we multiply the nightside sunlight and thermal maps by the relative intensity of each, as given by the normalized spectral intensity, and subtract this from every wavelength bin. This results in bin maps that should represent pure H_3^+ emission alone.
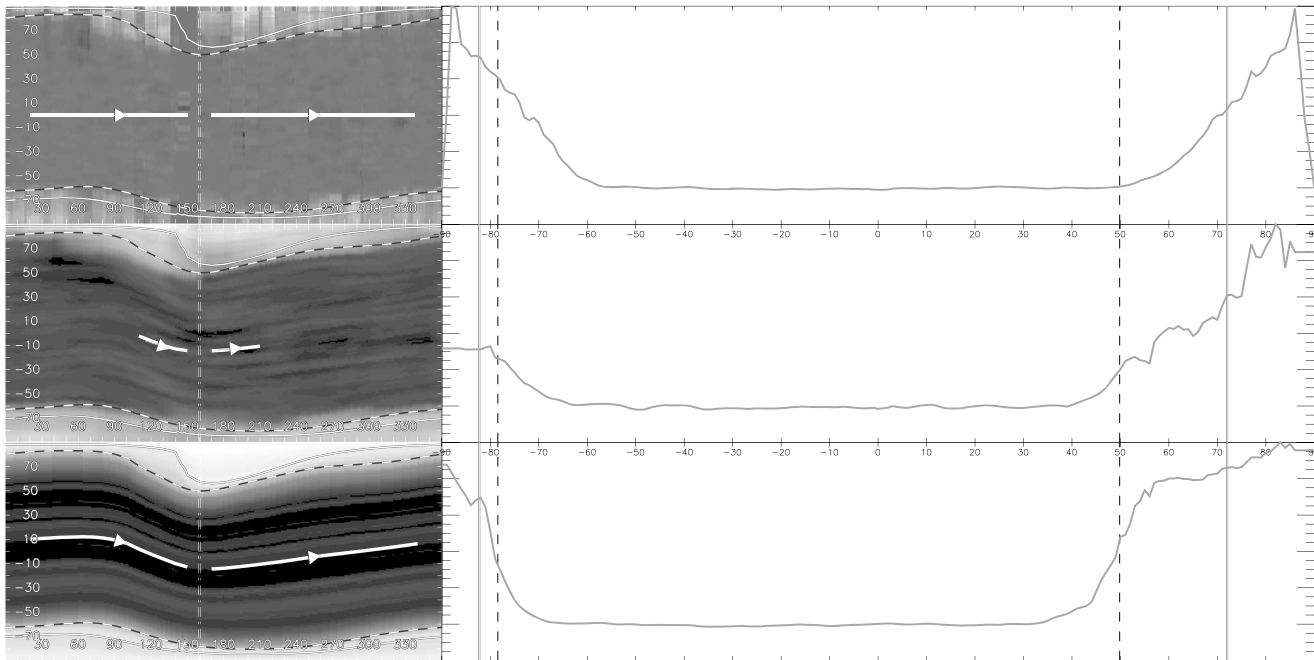
Figure 9. The three methods of summing data in the longitudinal direction, for bin 160. The (right) resultant profiles are affected by the shape of the (left) H_3^+ emission map, in particular the way the aurora changes in latitude due to the shape of the magnetic field mapping (taken from *Grodent et al.* [2008]: main auroral emission, 30 R_J, shown by solid white and Io aurora, 5.9 R_J, by dashed black and white). Summing along lines of (top) equal latitude results in a latitudinally distended H_3^+ emission. However, coadding the data using a linear mapping between the 30 R_J and Io mapping locations removes this smearing of the H_3^+ profile. Ultimately, it is better to average the intensity across (bottom) all magnetic longitudes, as it reduces observed noise further at the expense of understanding longitudinal variability.

In order to show how well this subtraction process has worked, we coadded the nightside intensity in latitudes 60–80°N and longitudes 159–227°W$_{III}$, in a region where the H_3^+ aurora is brightest. This produces a strong H_3^+ emission spectra, shown as the solid green line in Figure 8. We then calculated using the *Neale et al.* [1996] list of H_3^+ transition frequencies and intensities and the parameterization of the H_3^+ partition function of *Miller et al.* [2010], shown as the vertical green lines in Figure 8. When convolved to the resolution of VIMS, shown in Figure 8 as a dashed green line, the modeled H_3^+ spectra for a temperature of 900 K provide a very good fit for the measured intensities in the 3.2–4.3 µm wavelength range. The bin which observes bright P-branch H_3^+ emission line close to 4.4 µm (bin 209) has proven unreliable in the past, due to significant noise, and so we aviod it here. At wavelengths longer than 4.4 and shorter than 3 µm, all H_3^+ emission is obscured by the dominant solar-reflected sunlight and thermal emission, where the H_3^+ emission was weaker than spectral changes in the sulight and thermal maps produced. As such, we will limit our study to wavelengths where the H_3^+ emission is well measured, between 3.2 and 4.3 µm.

3.4. Longitudinal Coadding

The result of removing the background signal from each bin produces spectral maps within each bin theoretically containing only H_3^+ emission. However, these maps—an example of which is shown for the nightside H_3^+ from bin 160 in Figure 9 (top left)—remain relatively noisy. They have significant variability with longitude that is caused by the changing auroral conditions on short timescales over the time of this study. Since the VIMS flyby was relatively short, it is, unfortunately, not possible to track the conditions that produced this variability. However, it is important to smooth the data to remove these temporal changes. The emission structure varies far more quickly in latitude than longitude, and so it is preferable to smooth over longitudes. However, because the H_3^+ emission is latitudinally confined by magnetic fields, and Jupiter's magnetic pole is significantly offset, smoothing along lines of equal Jovigraphic latitudes results in a significant amount of latitudinal smoothing. The resultant profile produced by a longitudinal smoothing is shown in Figure 9 (top), where all auroral structure is lost.

In order to best smooth the H_3^+ emission in the longitudinal direction, we will instead smooth along lines of equal Jovimagnetic longitude. The simplest valid way to transfer from Jovigraphic to Jovimagnetic coordinates is to linearly interpolate between previously calculated locations of the Io spot and tail (mapping to 5.9 R_J) and the main auroral emission (mapping to 30 R_J), interpolating for each longitudinal position (D. Grodent, private communication, 2013; S. Cowley, private communication, 2013), smoothing along lines of equal magnetic latitude with changing Jovigraphic longitude. Although a more detailed mapping of the magnetic footprints of the Jovian moons has recently been produced by *Hess et al.* [2011], here we use the footprints defined by the *Grodent et al.* [2008] model, as these are given in regular steps of longitude. The specific model used is not important away from the auroral regions, as the magnetic field lines that map to these equatorward regions are largely dipolar.

For simplicity within this paper, we here define a nomenclature for Jovimagnetic latitudes that map to the main auroral emission at 30 R_J as 30°R_J and magnetic latitudes that map to Io at 5.9 R_J as 5.9°R_J. Jovigraphic System III latitudes and longitudes will be written in degrees north south and west, for example, 30°N, −30°S, and 160°W$_{III}$.

In order to convert between Jovimagnetic and Jovigraphic coordinates at different longitudes, we take the Jovigraphic latitudinal emission profile within any particular longitudinal position and split it into Jovigraphic latitudinal regions, with the edges of these regions defined by the north and south 30°R_J and 5.9°R_J locations by the positions of the northern and southern Io spot and 30 R_J mapping, resulting in five regions: north pole to north 30°R_J; north 30°R_J to north 5.9°R_J, north 5.9°R_J to south 5.9°R_J, south 5.9°R_J to south 30°R_J, and 30°R_J south to south pole. To convert the Jovigraphic latitudinal emission profile into the magnetic mapping at another longitude, each of these regions is linearly stretched to the size of the matching region at the new longitude.

Using this method, it is possible to interpolate along lines of equal Jovimagnetic longitude and so produce a boxcar smoothing along Jovimagnetic longitudes. In order to maintain longitudinal trends in H_3^+ emission, we perform a 30° longitude boxcar smooth, as shown in the middle map and profile of Figure 9, that we will use in the majority of this study. However, in order to maximize the signal to noise within the equatorial region, we also smooth the H_3^+ emission across the entire planet, producing a map of mean H_3^+ emission that is constant along lines of Jovimagnetic longitude; this is shown in the bottom map and profile of Figure 9 and will be used in sections 5 and 6.

## 4. Dayside and Nightside H_3^+ Emission Structure

Once we have performed all the processes detailed in the above section, it is possible to measure the mean intensity over the ranges of wavelength that H_3^+ emits to produces maps of H_3^+ emission on the dayside and nightside of the planet. Figure 10 includes four panels, which represent the dayside and nightside H_3^+ emission within two different wavelength ranges, each scaled to the power 0.7, in order to enhance lower level emission.

The two wavelength ranges used were selected for the following attributes:

1. A narrow wavelength range covering 3.197 and 3.530 μm, combining VIMS bins 140 to 160. These wavelengths, the narrow H_3^+ region shown in Figure 8, are where the combined reflected sunlight and thermal emission are weakest, producing the purest measure of the H_3^+ signal.
2. A broader wavelength range covering 3.197 and 4.315 μm, combining VIMS bins 140 to 207. This wavelength region, the extended H_3^+ region shown in Figure 8, is the region over which there is reasonable background subtraction on the nightside. This region has a broader spectral coverage, allowing a more accurate spectral fitting to be produced.

4.1. Quantifying the H_3^+ Emission Maps

Comparing the dayside and nightside H_3^+ emission for the narrower wavelength range (Figure 10, top) shows a similar overall structure, with the brightest emission concentrated at the poles, close to 30°R_J, fading at 5.9°R_J and dropping significantly at lower latitudes. However, even using the reduced wavelength range, there is significant noise in the equatorial region of the dayside image, with bright striations running across the
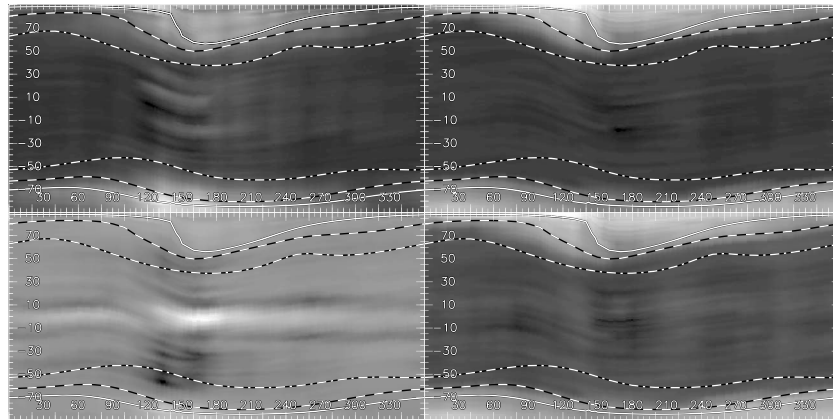
Figure 10. The H_3^+ emission maps for the (left) dayside and (right) nightside, covering two wavelength scales, a more restricted wavelength range of 3.197 and 3.530 μm (top; bins 140 to 160) which minimizes the effects of reflected sunlight and thermal emission and a wider wavelength range of 3.197 and 4.315 μm (bottom: bins 140 to 207) that provides a broader spectral coverage. These wavelength ranges are shown in Figure 8. Also shown are the magnetic latitudes that map to 30 R_J (solid line), 5.9 R_J (dashed line; Io), and 2.54 R_J (dash-dotted line; Amalthea); the first two using coordinates from the Grodent model [*Grodent et al.*, 2008] and the last from the VIP4 model [*Connerney et al.*, 1998].

center of the map. This suggests that the background reflected sunlight has not been fully removed from the dayside image. As such, our study will concentrate on the VIMS measurements of nightside emission.

The wider wavelength range is represented by Figure 10 (bottom). The dayside map for this range is dominated by the errors in our sunlight subtraction. However, for the nightside map, our sunlight and thermal emission subtraction have effectively removed the majority of the background. Comparing the nightside maps produced by the reduced and extended wavelength ranges, the overall morphology is clearly very similar. However, the extended wavelength map shows some regions of darkening and brightening in the equatorial region, perhaps indicative of slight errors in the thermal emission removal.

By comparing these maps, it is clear that our measurements on the dayside of the planet are relatively poor, and we will not use these maps in the following investigation. On the nightside, our calibrations have produced accurate maps of H_3^+.

The apparent emission at magnetic latitudes that map between Io (5.9 R_J) and Amalthea (2.54 R_J) could be the result of longitudinal broadening, caused either by large pixel size or by emission in the line-of-sight originating from a broader range oflongitudes. However, we estimate these affects would produce, at most, a smear of less than 10° in the nonauroral regions, far smaller than the extent measured here. In addition, since our data consist of cuts of the limb at nearly all longitudes, this bleeding would be expected to also occur at all longitudes and would stretch to both higher and lower longitudes. Since this effect is strongly asymmetric, this strongly suggests emission that maps equatorward of Io (5.9 R_J) is not caused by such smearing and can be interpreted as the result of true nonauroral emission.

Over the narrow wavelength range, this calibration is effective across the entire planet, and so this image will be used for discussing the relative emission of H_3^+, later in this section, as well as comparisons with the dayside emission in section 6. The wider wavelength range is accurate within both the auroral and subauroral regions but has higher noise close to the equator. We will use this extended wavelength range when investigating the upper atmosphere's physical conditions in section 5.

4.2. Nightside H_3^+ Emission Morphology

Concentrating on Figure 10 (top right), we see that the majority of H_3^+ emission is strongly concentrated in the auroral regions, with little emission observed at magnetic latitudes lower than 5.9°R_J. There is little obvious evidence for an extended region of mid-to-low latitude emission across all longitudes, with nonauroral regions all having effectively no H_3^+ emission. However, there is evidence that some subauroral latitudes show significant brightening in both the north and south but only over restricted longitudinal ranges. This subauroral brightening is most clearly seen in the north at longitudes of 60 and 160 and in
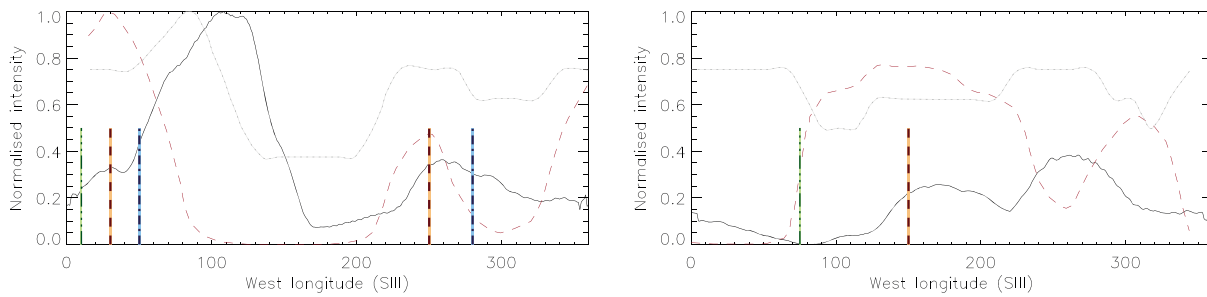
Figure 11. The normalized nightside H_3^+ emission (solid line) observed at magnetic latitudes between 2.54 and 5.9°R_J, plotted against longitude for the (left) north and (right) south. This is plotted against the normalized modeled e^-, H^+, O^+, and S^+ particle precipitation at 1.5°R_J, where the variation is maximized, as predicted by *Abel and Thorne* [2003] for the VIP4 magnetic model (red dashed line) [*Connerney et al.*, 1998]. Since peak precipitation coincides with magnetic minima, the approximate locations of magnetic minima are from the VIP4 model (red dashed vertical lines), the Grodent model [*Grodent et al.*, 2008] (blue dash-dotted vertical lines), and the VIPAL model [*Hess et al.*, 2011] (green dash-triple dotted vertical lines). Also shown is the normalized dayside H_3^+ emission at 1.5°R_J (dotted grey line; the only dayside H_3^+ value provided by the paper does not provide dayside values for higher magnetic latitudes) taken from the *Miller et al.* [1997] data and presented in *Abel and Thorne* [2003].

the south at longitudes of 240 and 300. For both the north and south, this represents a region that sits at longitudes shorter than the region where the aurora extends to its lowest latitudes.

This apparently asymmetric subauroral emission appears to map to a magnetospheric location between ~3 and 4 R_J and 5.9 R_J. Although "ribbon aurora" has been speculated for this region [*Rego et al.*, 1999], it only occurs under extreme conditions, for short periods of time, and is confined to a region only 0.2 R_J closer to the planet than Io, and so it is unlikely that discrete auroral processes produce the subauroral emission.

It is possible that the emission measured is diffuse auroral emission driven by pitch angle scattering of energetic particles. *Abel and Thorne* [2003] showed that particle precipitation flux for e^-, H^+, O^+, and S^+ are all inversely proportional to the magnetic field strength. In Figure 11, we compare the normalized emission intensity (the solid line) from magnetic latitudes between 2.54°R_J and 5.9°R_J (the dashed and dash-dotted lines in Figure 10) with the predicted particle precipitation flux for 1.5°R_J, where the largest variations in precipitations are largest (the dashed red line). Values for the normalized emission intensity within the 1.5°R_J region were also measured, but unfortunately no clear H_3^+ signal could be distinguished from the background. Flux values are provided within *Abel and Thorne* [2003] for electrons only, with no values for H^+, O^+, and S^+ at 2°R_J and 4°R_J; however, the electron values show that the flux shows a similar overall intensity strength and general structure at all magnetic latitudes, but the variation in flux with longitude is strongest at 1.5°R_J, becoming smaller in longitudinal variation at higher magnetic latitudes. We also compare the nightside intensities measured here with normalized dayside intensities measured at magnetic latitudes that map to 1.5°R_J that were presented in *Abel and Thorne* [2003] but were taken from *Miller et al.* [1997] and provided to them by that author (the grey dotted line).

Our observations of the nightside H_3^+ emission share a broadly similar intensity structure to the dayside emission observed by *Miller et al.* [1997], though the intensity varies much more strongly with longitude on the nightside, perhaps because the dayside emission includes a significant amount of H_3^+ generated by solar EUV ionization. One notable difference is that the strongest peaks we have identified of nightside emission, at longitudes of ~110°W_{III} in the north and ~260°W_{III} in the south, are far brighter than the secondary peaks, at ~260°W_{III} in the north and ~170°W_{III} in the south. On the dayside, these primary and secondary peaks are relatively similar in intensity. These differences may be because we are sampling higher magnetic latitudes in the nightside data. The lack of emission at 1.5°R_J, where the precipitation modeled by *Abel and Thorne* [2003] is similar in magnitude but with greater longitudinal variations, may indiciate that the observed emission between 2.54°R_J and 5.9°R_J is driven by other processes, or it may indicate that emission in this region is suppressed by lower temperatures.

Comparing our northern emissions with the predicted regions of northern particle precipitation shows that both the overall structure and relative intensity of primary and secondary emission peaks appear to follow the modeled flux well, though there is a significant offset between the brightest peak and strongest flux. However, the southern emissions do not match at all well with the predicted particle precipitation in

overall structure, relative intensity at different longitudes, or the predicted emission when compared with the north. This mismatch in the south was noted in *Abel and Thorne* [2003] but is even clearer here.

Currently used models of the Jovian magnetic field (VIPAL from *Hess et al.* [2011]; Grodent from *Grodent et al.* [2008]; VIP4 from *Connerney et al.* [1998]) all disagree on the exact location of weakest magnetic field strength in the subauroral region, and so it may be that in using the VIP4 model, *Abel and Thorne* [2003] placed the region of highest emission in the incorrect location. In order to test this, using Figure 2 in *Hess et al.* [2011] as a guide, we have placed an approximate location of weakest field strength from each of the three models into Figure 11 (red dashed vertical line for VIP4, blue dashed vertical line for Grodent, and green dashed vertical line for VIPAL). In the north, all the models produce magnetic field minima at similar longitudes, though the Grodent model does sit closer than the others, a result of the more significant distortion needed to best fit the main auroral oval location. For the south, the more circular lines of equal magnetic latitude result in smaller overall variations in the field strength, but the VIPAL and VIP4 models (the Grodent model only investigated the northern aurora) have very large differences in the shape that the magnetic field strength takes in the nonauroral regions. The uncertainties in these models could potentially allow the measured intensity structure to be entirely the result of diffuse aurora. Assuming that diffuse auroral processes produce the sub-5.9°R_J H_3^+ emission measured here, further investigation of the exact location and strength of this emission could prove highly useful in future modeling of the magnetic field.

One caveat to an auroral origin for the subauroral H_3^+ emission is that matching auroral emission is not clearly observed within UV images at Jupiter, although there is evidence that the H_2 UV dayglow cannot be entirely accounted for by solar EUV [*Feldman et al.*, 1993]. One possible explanation for the lack of such emission within dayside UV images is that weak emission away from the auroral region is sometimes difficult to observe in UV images, as the breadth of the UV filters used results in significant reflected sunlight and so requires very careful background subtraction; it is possible that this subauroral emission is too weak to observe clearly.

Alternatively, this H_3^+ emission may not represent a direct auroral process at all and instead may be indicative of strong auroral flows away from the auroral region. Observations of the ionospheric flows within Jupiter's auroral region have shown that the main auroral oval has an ion wind with speeds of 0.5–1 km/s flowing against corotation [*Stallard et al.*, 2001], while the dawnside of the polar region is strongly affected by the solar wind, resulting in regions that are held at an inertial zero velocity [*Stallard et al.*, 2003]; these stationary ions appear, in the planetary frame, to have ion wind velocities as high as 4 km/s, again flowing against corotation. These strong subrotational flows could represent the transport of H_3^+ over distances of up to 2500 km, assuming a H_3^+ lifetime of 10 min [*Tao et al.*, 2011]; this would result in a longitudinal motion of 3–5°W_{III}, so that this feature can only be partially explained by the direct transport of H_3^+. Another argument against this transport of H_3^+ is that a combination of Joule heating and subauroral magnetic fields will act to reaccelerate the H_3^+ back to corotation. However, the strong subrotational driving force within the auroral region might also drive a powerful neutral wind, which in turn could help transport H_3^+ ions away from the auroral region along lines of equal Jovigraphic latitude.

5. Physical Conditions

H_3^+ emission, under local thermal equilibrium, emits as a function of both the temperature of the surrounding thermosphere and of the number of molecules within the column observed in the line-of-sight of the observation. By measuring the spectral characteristics of the H_3^+ emission, it is possible to separate out these contributions and use them to calculate how the H_3^+ is cooling the surrounding atmosphere.

In section 4, we compared the relative intensities of the dayside and nightside aurora but have avoided using specific values for intensity. This is because unlike high spectral resolution observations of H_3^+ from ground-based telescopes, it is not possible to resolve individual line intensities using VIMS. This is because the low spectral resolution provided by VIMS produces a spectral measurement at any particular wavelength that consists of multiple H_3^+ emission lines, as can be seen in Figure 12. Since these individual lines represent rovibrational transitions of different energies, and the difference in relative brightness of these lines changes with temperature, to extrapolate a meaningful line intensity requires a measurement of the temperature. This is additionally confused, as the farther each emission line sits from the center of a
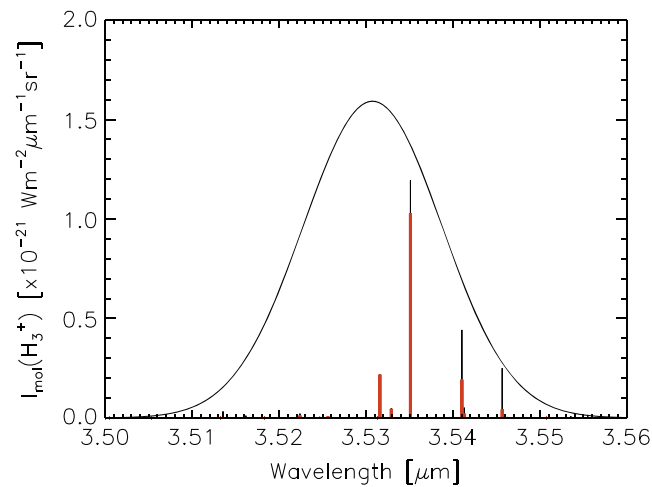
Figure 12. The line intensities for all H_3^+ transitions between 3.50 and 3.56 μm for an individual H_3^+ molecule at 1180 K (black vertical lines) and the intensity of these lines when measured by the VIMS instrument in wavelength bin 160 (vertical red lines), which, like all VIMS bins, has a Gaussian sensitivity (the Gaussian shown has the FWHM for bin 160 and a peak height that is the combined VIMS scaled line intensities for bin 160).

VIMS wavelength bin, the more the observed line intensity is reduced, by a Gaussian function with a known full-width half-maximum (FWHM) that differs for each wavelength bin. As such, it is more useful, and more meaningful, to model the individual line intensities simultaneously across the entire H_3^+ region. In this section, we will calculate how individual line intensities produce a modeled VIMS spectrum and compare this to the measured VIMS spectra that contributes to the intensity map shown in the section 4, producing a fit for temperature and thus H_3^+ density and total emission.

5.1. Measured VIMS Intensity

The H_3^+ emission maps presented in the section 4 were produced by summing the H_3^+ emission across either a narrow or extended wavelength range.

The limited spectral resolution of VIMS means that to properly calculate the physical conditions in Jupiter's upper atmosphere, we will need to use as wide a wavelength range as is possible. As such, we will use the extended wavelength range here, coadding emission from the VIMS wavelength bins 140–207, in effect approximately measuring the H_3^+ total emission across the wavelength range 3.197 and 4.315 μm.

Even with this extended range, the accuracy of fitting remains somewhat limited and so we will initially measure the physical conditions using an emission map that has been smoothed across all Jovimagnetic longitudes, producing a longitudinally averaged emission map (as shown in Figure 9 (bottom)). It is from this emission map we will calculate temperature, column density, and total emission across Jupiter's ionosphere.

We also produce a latitudinal profile of emission using this map, measuring the emission at longitudes that cut through the northern and southern auroral regions at longitudes where each aurora extends to low latitudes, to provide as broad a view of these aurora as possible. For this, we have produced an intensity profile that combines the latitudinal variation in emission along a longitude of 160°W$_{III}$ in the north and 20°W$_{III}$ in the south. The longitudinally averaged emission map, with these locations marked, and the resultant latitude emission profile are shown in Figure 15 (top), which will be discussed in section 5.6.

While smoothing across all magnetic longitudes produces a more accurate measure of the latitudinal variation atmospheric physical conditions, it limits our ability to assess the origin of longitudinal variations in emission, in particular the strong variation in subauroral emission shown in Figure 11. In order to understand what is driving the formation of these features, we will use the emission map smoothed over only 30° of Jovimagnetic longitudes (the emission map shown in Figure 10 (bottom right)). As this map has a lower signal to noise, the resultant calculated physical conditions will have significantly higher associated errors, and so care will be needed when interpreting the results from these maps. Since we are most interested in calculating the physical conditions in the regions that subauroral emission is strongest, we have produced an emission profile that follows the emission map at a longitude of 110°W$_{III}$ in the north and 250°W$_{III}$ in the south. The longitudinally varying emission map, with these locations marked, and the resultant latitude emission profile are shown in Figure 16 (top), which will be discussed in section 5.7.

Using the variation in emission measured within the equatorial regions of the profile, between 40°N and −40°S, we calculate the standard deviation in our intensity measurements, to produce an error in intensity, shown in
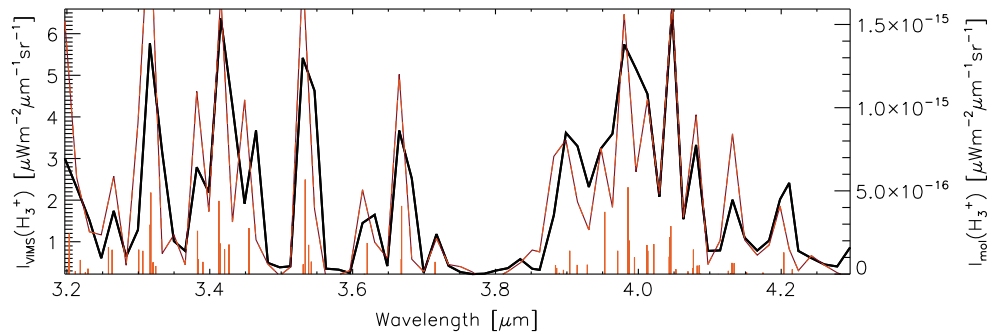
Figure 13. The measured H_3^+ emission spectra (I_{VIMS}; thick black line) at a latitude of 70°S and a longitude of 20°W_{III}, using a magnetic longitude smoothing of 30°. This is plotted against the modeled intensity measured by VIMS assuming a rotational temperature of 1180 K, with specific intensity scaled across the rotational population to the effective emission from one molecule of H_3^+ within each wavelength bin (I_{mol}; red line), with each wavelength position representing the intensity calculated for that bin, as shown by example in Figure 12. Also shown are the individual H_3^+ emission lines in this region (vertical orange lines; these are scaled down by a factor of 2 for clarity).

the profiles in Figures 15 and 16 as a shaded region. This error is small, and neglects that variations measured in the equatorial region are real, and so may overestimate the error in intensity.

5.2. Fitting Temperature

Past observations of H_3^+ emission from Jupiter has shown that it exists in quasi-local-thermal-equilibrium [*Miller et al.*, 1990], so that the radiative deexcitation of vibrational excited states occurs more slowly than this excitation is refilled by collisions with the surrounding H_2 atmosphere. As such, for a given temperature the relative brightness of each rovibrational line will be the same, and measuring the different intensities of these lines within a spectra will allow a direct fit of the temperature of the surrounding neutral atmosphere. However, fitting individual line intensities is not possible using VIMS, as the spectral resolution of the instrument is too low to resolve these individual lines. Instead, it is necessary to calculate the expected total emission within each individual VIMS bin across the range of temperatures that we expect from Jupiter, in order to produce a modeled VIMS H_3^+ emission spectrum.

Figure 12 shows how an individual bin emission intensity is calculated. Firstly, the line intensities from a single molecule of H_3^+, within the region of the wavelengths covered by the bin, are calculated for a given temperature (in this case 1180 K). The intensity of each line is then reduced by the Gaussian response of that VIMS bin, using the distance between the central wavelength of the bin and the wavelength of each line to scale the line emission by the normalized Gaussian height of the bin at that position. These individual scaled line emissions are then summed to produce an expected VIMS-observed intensity per molecule (I_{mol}) for that particular temperature.

The central wavelength and FWHM of each bin have been calculated both from laboratory measurements before launch and by calibration in-flight [*Brown et al.*, 2003] and are listed in the header information for each data file; it should be noted that recent observations have suggested the VIMS central wavelengths have shifted during the Cassini mission, but that these shifts occur only at Saturn, and the wavelength calibration is unshifted at Jupiter.

By calculating the intensity I_{mol} for each VIMS bin between 140 and 207, it is possible to produce a modeled VIMS spectrum for any particular temperature, which directly correlates to the H_3^+ spectra measured by VIMS (I_{VIMS}). Although the emission brightness of these spectra is magnitudes apart, the relative strength of each wavelength bin is the same for a given temperature, as can be seen in Figure 13. In order to produce a fitted temperature for a particular VIMS spectra, we calculate the expected intensity I_{mol} between 100 K and 2000 K in steps of 1 K. We then normalize both the modeled and measured spectra to a fractional intensity by dividing each by the total intensity across all the wavelength bins (so that all bins added together now sum to one).

This removes the magnitudinal differences between the modeled and measured spectra (which we will return to in the section 5.3) and allows us to use a minimum difference method, subtracting the modeled intensity for each temperature step from our measured intensity, and find the temperature with the least residuals. We perform this fit for every latitude and longitude position in the emission map, to produce a temperature map, and then measure the latitudinal profile for this map in the same way as for emission. This results in a temperature map and latitudinal profile for the longitudinally averaged data shown in red in the second from Figure 15 (top) and for the longitudinally variable data shown in Figure 16, discussed in sections 5.6 and 5.7.

As the emission brightness of H_3^+ drops, it becomes impossible to produce an accurate measurement of the temperature. As such, we have filtered the temperatures so that when the measured VIMS intensity is less than 5% of the peak emission, we set the temperature matching that location to the minimum measured temperature. This is shown in Figures 15 and 16 as a dashed orange line, and typically only covers latitudes significantly equatorward of $5.9°R_J$. We have used this fixed temperature in subsequent physical parameter calculations.

In order to understand the errors associated with our fitted temperatures, we take the measured residuals for each fit, take the modeled spectrum for this temperature, and randomly add this level of residual back into the spectrum, using a uniform distribution of noise across all wavelengths. We then refit the noisy spectrum with a new temperature. We repeat this process 100 times for each fit and then measure the standard deviation in the noisy temperatures—it is this standard deviation that we use as our temperature error, shown as the shaded orange region around the temperature profile in Figures 15 and 16.

5.3. Calculating Column Density

In the section 5.2, we factored out the magnitudinal differences in the calculated and measured H_3^+ emission in order to fit a temperature. This large difference between the intensities comes as a result of modeling the emission per molecule and measuring the overall emission from the ionosphere, and so once we have calculated the temperature, the scaling between these values effectively gives a measure of the column integrated density of H_3^+ ions within the line-of-sight.

As such, producing a value for the column density is a simple matter of dividing the total intensity in the measured spectrum by the total intensity in the modeled spectrum. However, this produces a measure of the number of molecules observed by VIMS as it looks at the limb of the planet. The glancing angle that is associated with VIMS's view of the limb of the planet results in a strong increase in the amount of atmosphere observed when compared with the center of the planet; this enhancement is the reason this study has concentrated on limb emission, as it produces brighter H_3^+ emission than on the planet. However, to produce an accurate measure of the density of H_3^+ in a vertical column of the atmosphere, we must model and correct for this limb enhancement.

For simplicity we model the H_3^+ with the ionosphere uniformly with latitude, as shown in Figure 14. In this model, we use Jupiter's mean radius of 69,911 km and assume that the planet is opaque below this 1 bar level and transparent above this 1 bar level (shown in Figure 14 as the grey region) and that the H_3^+ is uniformly distributed in a shell between 300 and 500 km above the 1 bar level, which is the approximate location of the peak H_3^+ emission according to current models [e.g., *Tao et al.*, 2011]. In our calculations, we assume a Jupiter is a sphere, as the differences in line-of-sight enhancement produced in an oblate model are insignificant on the scale of an individual pixel. From this, we calculate the altitudinal enhancement of the H_3^+ emission over what would have been measured at the equator across the ±5000 km range of distance from the limb used in this study, as shown in Figure 14 (right). We acknowledge that this is a simplistic model of the upper atmosphere, but given the poor constraints on the true structure within this region, it allows us to calculate an approximate value for the overall enhancement. When the resultant line-of-sight enhancement is integrated between −5000 and +5000 km, it produces an overall enhancement of 3.282, which we round to 3.5 for simplicity. We assume that this approximate line-of-sight enhancement is the same at all latitudes measured.

Reducing the measured H_3^+ emission by this line-of-sight factor results in a measurement of the H_3^+ emission from a vertical column integrated square meter of atmosphere, so that when this is divided by the emission from a single molecule of H_3^+ at the measured temperature, we calculate the H_3^+ column density. Using this,
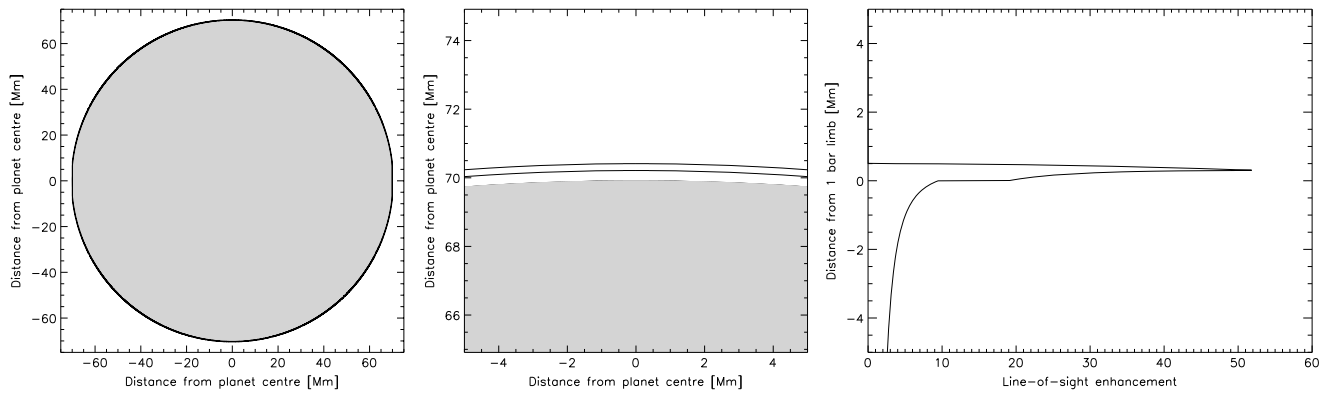
Figure 14. The line-of-sight path measured within 5000 km of the limb of the planet, as viewed from above. We model the atmosphere as opaque below the 1 bar level, and the H_3^+ emission as uniform between 300 and 500 km above the 1 bar level. These are shown for the (left) entire planet and over the ±5000 km range used in (middle) this study, with the opaque planet in grey, and the emission region between two black lines. (right) Line-of-sight enhancement observed through the atmosphere, producing a mean enhancement of ~3.5 across the entire +5000 to −5000 km range.

we have calculated a column density map and latitudinal profile, for the longitudinally averaged data, shown in blue in the third from Figure 15 (top), and for the longitudinally variable data shown in Figure 16, discussed in sections 5.6 and 5.7.

Since our fit of temperature has a far larger error associated with it than the measured H_3^+ emission, we have produced a measure of the H_3^+ column density by calculating what the column density would be if the measured temperature had the standard deviation in temperature added or subtracted from it. This error is shown as a shaded blue region in the profiles in Figures 15 and 16.

5.4. Calculating Total Emission

Calculating the total emitted light from H_3^+ across all wavelengths provides a measure of the H_3^+ cooling rate to space. Assuming local thermal equilibrium, this H_3^+ total emission, $E(H_3^+)$, is measured by calculating the total emission per molecule, $E_{mol}(H_3^+)$, and factoring this against the H_3^+ column density [*Lam et al.*, 1997]. In this paper, we use a recent parameterization of the variation in total emission from a single molecule with temperature that was presented in *Miller et al.* [2013], using the new parameterization for the partition function presented in *Miller et al.* [2010]. Using this, we can use our temperature maps to calculate the $E_{mol}(H_3^+)$ at each latitude and longitude position and then factor this against the matching column density map in order to produce a H_3^+ total emission map and latitudinal profile, for the longitudinally averaged data, shown in green in Figure 15 (bottom), and for the longitudinally variable data in Figure 16, discussed in the follow two sections.

The total emission parameter was originally produced by *Lam et al.* [1997] in order to produce a value with minimal errors, since fitted values of temperature and column density are often anticorrelated with one another. However, while calculations of the errors in temperature and column density are typically dominated by this anticorrelation [*Melin et al.*, 2014], we have no way to fully assess whether this is the case here. As such, we use the temperature errors to calculate our total emission error, shown by the shaded green region in Figures 15 and 16. However, these should be taken as upper values for error, since it is likely that in factoring temperature against column density, we have removed the anticorrelation in the fit and thus significantly reduced the errors seen here.

5.5. Hemispheric Power Output

Using the longitudnally varying maps of total emission shown in Figure 16, it is possible to calculate the total auroral output within each hemisphere. Here, we have simply averaged the total emission across each hemisphere and factored it against the total surface area. The spike in emission found in the northern pole is likely to be an error caused by sunlight from the dayside, and so we have limited the maps to 1.5 mWm^{-2} when calculating the hemispheric total power. This results in total integrated H_3^+ auroral output of 7.6 ± 0.4 TW from the northern hemisphere and 5.2 ± 0.3 TW in the southern hemisphere. These
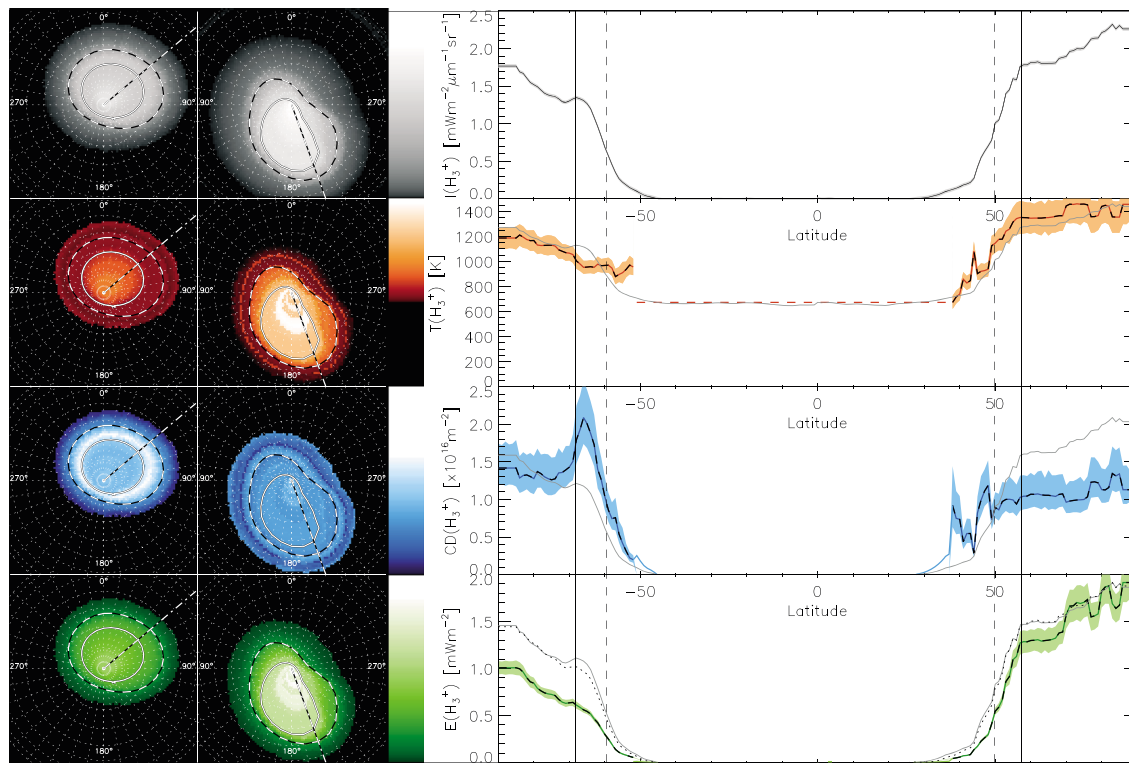
Figure 15. The Jovimagnetic longitudinally averaged nightside H_3^+ physical parameters, VIMS H_3^+ emission intensity ($I(H_3^+)$; first panel, greyscale), H_3^+ temperature ($T(H_3^+)$; second panel, red), the H_3^+ column density ($CD(H_3^+)$; third panel, blue), and H_3^+ total emission ($E(H_3^+)$; bottom panel, green). Each panel shows the paramater mapped from above the rotational pole (left; southern map on the far left, with the northern map to the right of it). The longitude location of the latitudinal profile marked (dash-dotted line), and the profile for this line of longitude is then shown on the right. Also shown overlain on the maps and as vertical lines in the profiles are the magnetic latitudes used to produce the magnetic summing, taken from *Grodent et al.* [2008], for 30 R_J (solid line) and 5.9 R_J (Io; dashed line). A brightness scale is also shown for each map, scaled to the y axis for each corresponding profile.

values are moderately higher than *Lam et al.* [1997], who measured ~3 TW emitted from each hemisphere, but remains similar to total output from UV auroral emission and up to an order of magnitude lower than IR hydrocarbon auroral emissions [see *Bhardwaj and Gladstone*, 2000]. The auroral output clearly dominates the combined total power; we estimate the total hemispheric power from H_3^+ generated by solar EUV as ~0.15 TW per hemisphere, based upon the comparative values estimated in Figure 17.

5.6. Latitudinal Variation in the Physical Conditions

Immediately clear from both the maps and profiles in Figure 15 is the well-established fact that the H_3^+ emission at Jupiter is strongly dominated by the auroral region. Our measured H_3^+ emission (Figure 15, top) is strongest at the poles, perhaps with the inclusion of a sunlight component in the most poleward latitudes, but with a clear peak in both poles at the location of 30°R_J (denoted by the solid vertical lines). Equatorward of these latitudes, the emission strongly drops away, tapering off to almost nothing ~10° equatorward of 5.9°R_J (denoted by the dashed vertical lines).

As has been seen in past observations of Jupiter's dayside [*Lam et al.*, 1997; *Stallard et al.*, 2002; *Raynaud et al.*, 2004; *Lystrup et al.*, 2008], the nightside temperature is relatively stable within the auroral region, with our measurements of auroral temperatures between 1000 K and 1400 K well within those measured on the dayside of the planet. It appears that the brighter emission seen in the poles is driven largely by the slightly higher temperatures within this region, though this raised polar heating is typically less than the errors in our temperature fitting.

We know from modeling of the heating and cooling of the auroral region [*Melin et al.*, 2006] that the temperature of the upper atmosphere is dominated by Joule heating by auroral currents, while the solar contribution to heating is negligible [*Yelle and Miller*, 2004]. Joule heating covers a broader region than the
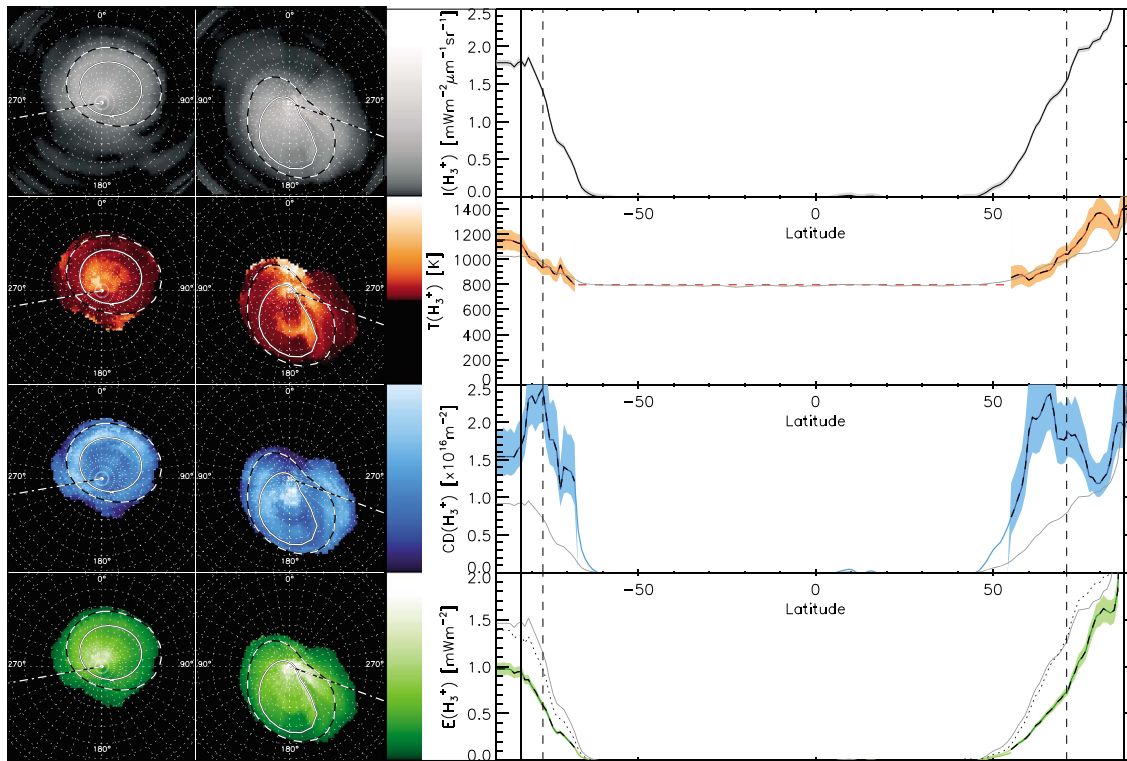
Figure 16. The Jovimagnetic longitudinally variable nightside H_3^+ physical parameters, as in Figure 15, but here showing the results of smoothing over 30° of Jovimagnetic longitude. Here, we highlight the subauroral emission, shown in Figure 11 to peak at 110 W in the north and 20 W in the south.

localized particle precipitation that drives the formation of H_3^+ (as well as prompt auroral emission in UV wavelengths), and so thermal variations are expected to vary over broad spatial scales. Since Joule heating is proportional to the conductivity, the lack of significantly different temperatures between the dayside and nightside of the planet suggests that the solar component of conductivity in the auroral region is insignificant, and it is the auroral conductivities that dominate, as has previously been modeled [e.g., by *Achilleos et al.*, 1998].

Away from the auroral region, the temperatures appear to drop away significantly, down as low as ~750 K at latitudes below 5.9°R_J. This temperature structure is in strong agreement with measurements by *Lam et al.* [1997], who observed a similar drop in temperature, before a slow increase back to ~950 K at the equator. It contrasts strongly with the subauroral temperatures observed by *Lystrup et al.* [2008], who observed an increase of 200 K at latitudes equatorward of the main auroral emission.

The nightside column density in the auroral region is between 1 and 1.5×10^{16} m^{-2}, again well within previous measurements [*Lam et al.*, 1997; *Stallard et al.*, 2002], unsurprising as the dayside column density is dominated by auroral ionization. As with temperature, this drops away at subauroral latitudes, though there is clearly a region of raised H_3^+ densities at latitudes below 5.9°R_J, especially in the north, which are suggestive that emission in this region is driven by increased H_3^+, rather than as a response to heating.

Finally, the nightside total emission measured between 0.001 and 0.002 Wm^{-2} in the auroral region, again in broad agreement with past dayside values. Equatorward of the auroral regions, the total emission drops away quickly, as a function of the decreasing temperature and column density. Interestingly, the total emission appears significantly brighter in the northern aurora than the south, the result of the significantly higher temperatures observed in this region. This may be indicative of increased heating in the north, perhaps as a result of the subrotational flows driven by solar wind interactions, which are stronger in the north as a result of the asymmetry in the magnetic field [*Stallard et al.*, 2001]. Alternatively, the temperature measurements in the north appear to have significantly higher errors associated with them, and this may be overestimating both temperatures and thus total emission.
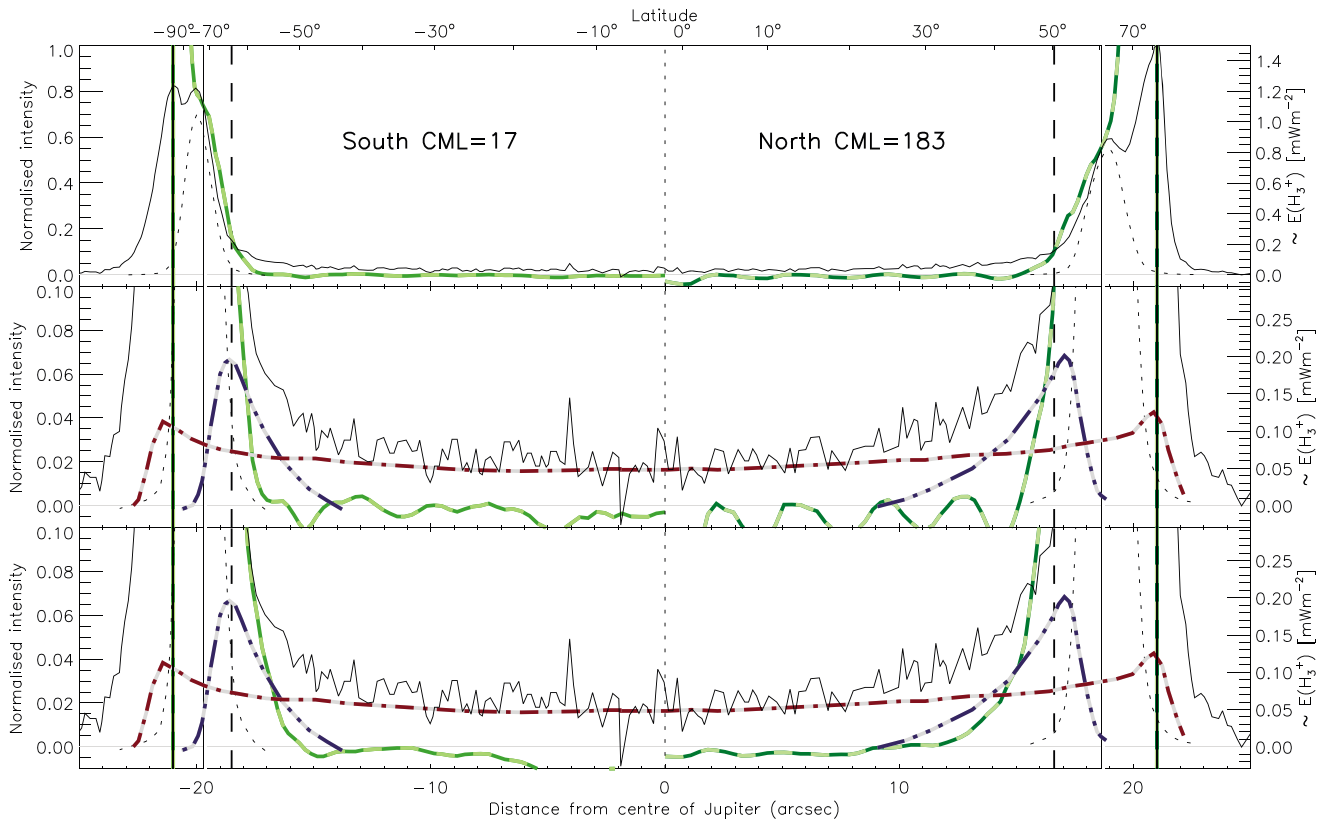
Figure 17. A direct comparison between dayside and nightside emission. (top) Dayside emission (solid line) taken from *Rego et al.* [2000]. The nightside emission (bold green dashed line) is taken from our study at longitudes that match with the data from *Rego et al.* [2000], using the H_3^+ emission smoothed along 30° of magnetic longitude, which is then converted using a method detailed in the text. Also shown are the magnetically mapped locations of 30 R_J (vertical solid double line) and Io (vertical dashed line), and the position of the limb (vertical bold line). (middle) Same dayside and nightside intensity profiles plotted on a reduced intensity scale. Also shown for comparison are the *Rego et al.* [2000] modeled mid-to-low latitude emission (blue dash-triple dotted line) and EUV ionized emission (red dash-dotted line) profiles. (bottom) The same dayside profiles, but replace the nightside profile with a converted profile of H_3^+ emission smoothed over all magnetic longitudes, using the smoothing shown in the bottom panel of Figure 9.

Comparing the latitudinal structure of the total emission with that of the measured VIMS intensities, the main difference appears to be this north/south total emission asymmetry, which is not as noticeable in the measured intensity. However, in terms of smaller scale emission, the structures of each are very similar, true for the measured emission from both the extended wavelength range (3.197–4.315 µm, in Figure 15 (bottom) as a normalized grey line) and the narrower range used in sections 4 and 6 (3.197–3.530 µm, shown in Figure 15 (bottom) as a normalized dotted line). This similarity comes from the broad wavelengths covered by the VIMS intensities, typically covering multiple emission lines from different energy levels. In effect, VIMS is measuring the total emission over a restricted wavelength range, and so while underestimating the absolute emission, it is better than single emission lines at approximating the overall total emission. We will utilize this similarity in the section 6, to approximate the total emission from the measured H_3^+ emission.

5.7. Longitudinal Variation in Physical Conditions

In Figure 16, we use the measurements of the physical parameters when the Jovimagnetic longitudes are only smoothed by 30°. This results in more variable and error-prone values for each physical parameter, but maintains enough longitudinal structure for us to examine what drives, in particular, the subauroral emission that Figure 11 shows to peak at 110°W_{III} in the north and 260°W_{III} in the south.

The measured emission structure is dominated by a spike of emission near the Jovigraphic north pole. At 110°W_{III}, the main auroral emission is very close to the Jovigraphic pole and coincides with this brightening. This coincidence may have introduced errors, and although bright arcs and spots of emission are both seen on the dayside main UV emission, especially in the dawn sector [*Grodent et al.*, 2003a],

but these do not always translate into H_3^+ emission [*Radioti et al.*, 2013]. Beyond that, the overall structure is similar to that seen in Figure 15, though emission appears to extend 20° equatorward of $5.9°R_J$, 10° further than the longitudinally averaged profile.

There is no evidence that this extension in the H_3^+ emission comes from a localized increase in the temperature. Temperatures continually decrease through the main auroral emission at $30°R_J$, with no increase equatorward of $5.9°R_J$.

However, the H_3^+ column density in the same region shows very strong enhancement in this region. At least some of this enhancement is likely to be associated with the Io spot and tail, but equatorward of this, there are significantly raised column densities. Given the restrictions of this particular data, specific values associated with this region may not be realistic. However, what is clear is that the raised emission noted in section 4 is driven by the presence of a localized increase in H_3^+. The increased column density may be a result of localized ionization, indirect production, or some transport process. It is obviously not produced by the production or transport of heat into this region.

Again, the total emissions match closely with the measured H_3^+ intensities, with some increased subauroral emission, but the significant enhancement in column density is partially countered by the decreasing temperatures.

6. Dayside and Nightside Comparisons

Past observations of H_3^+ emission from Jupiter have been solely made from the dayside of the planet, and in order to properly understand the emission we have observed on the nightside, it is useful to directly compare the dayside and nightside emission. However, our measurements of the dayside H_3^+ emission retained a significant component of reflected sunlight, as shown in Figure 10. Thus, in order to provide a detailed comparison of the H_3^+ emission on the dayside and nightside, we will need to compare our observations with past ground-based measurements.

6.1. Comparison With Ground-Based Data

Rego et al. [2000] presented ground-based observations of pole-to-equator Jovian H_3^+ emission profiles and then modeled the measured emission using a multi-emission-component model. These observations, taken using the CSHELL instrument on IRTF on 13–16 July 1996, presented two specific cases for the pole-to-equator emission profile: a northern hemisphere profile taken at a Central Meridian Longitude (CML) of 183 and a southern hemisphere profile at a CML of 17. The specific emission components for each of these emission profiles were modeled, and these two profiles represent the only detailed measurement of the relative intensity of the mid-to-low latitude emission within the scientific literature.

The *Rego et al.* [2000] paper does, however, have some significant limitations that will need to be accounted for before we can properly compare the two data sets:

1. The intensity profiles are plotted in arcsec distance from the center of planet.
2. No correction for line-of-sight enhancement was made.
3. The intensities are measured in arbitrary units, with no calibration provided, and so can only be examined as a measure of relative intensity across the central meridian.

In order to properly compare our data, we have taken our map of H_3^+ emission, which uses a narrow range of wavelengths (3.197–3.530 μm, from VIMS bins 140 to 160, as shown in Figure 9 (top right)). From this map, we have measured latitudinal intensity profiles at a west longitude of 183 (in the north) and a west longitude of 17 (in the south) to produce a north and south profile and have adapted these profiles to the above problems in the following way:

1. We have converted our latitudinal profile into coordinates that map our data onto an ellipsoid with Jupiter's 0.0648 polar flattening and the −2.01 sub-Earth latitude and 46.97 arcsec equatorial diameter observed in 1996.
2. We have applied an artificial line-of-sight enhancement to our data. Since the *Rego et al.* [2000] observations are along the central meridian, the line-of-sight enhancement is largely a function of cosine of latitude on the planet, accounting again for the sub-Earth latitude given above. We have applied this simple enhancement, resulting in increased intensity at the poles.

3. Jupiter's main auroral oval is relatively constant in both temperature and column density, and the power of the mid-to-low latitude emission appears to scale with the main auroral emission [*Morioka et al.*, 2004]. This allows us to make an assumption of equivalency in the brightness of the main auroral emission in the two intensity profiles in order to test the relative brightness of mid-to-low latitude emission between the dayside and nightside of the planet. We have normalized the *Rego et al.* [2000] intensity profiles, and then scaled each of our measured intensity profiles, so that the intensity on the main auroral oval matches in both the north and south.

Away from the auroral region, we have not been able to measure the physical conditions in the atmosphere and so cannot provide a direct measure of the H_3^+ emission intensity. However, in Figure 15, it is clear that while there are some spatial differences between the measured H_3^+ emission I_{VIMS} and the total emission $E(H_3^+)$, the intensity measured by VIMS can be used as a broad approximation of the total emission. As such, we can calculate a mean scaling between the mean I_{VIMS} and mean $E(H_3^+)$ in order to produce an approximation for the total emission from our measured intensities. Using the ratio of the totalled measured intensity and total emission within the profile shown in Figure 15, we calculate a scaling factor of 0.66. However, since we are observing the H_3^+ over the restricted 3.197–3.530 μm range, rather than the extended 3.197–4.315 μm range used in section 5, there is an additional 2.754 scaling for the reduced emission from these lines. This results in a combined scaling that factors our measured narrow I_{VIMS} by 1.82 to produce an approximated $E(H_3^+)$ emission value for both profiles.

The normalized dayside and nightside emission are plotted together in Figure 17, indicated by the black solid and green dashed lines, respectively, in three panels. Figure 17 (top) shows the full dayside intensity compared with the nightside emission, smoothed in longitude over 30°, measured at the same longitude; Figure 17 (middle) shows these same profiles scaled to 10% emission; and Figure 17 (bottom) again shows 10% emission but compares the dayside emission with the average emission across all longitudes. Estimated total emission values are given on the righthand *y* axis of the figure.

6.2. Auroral and Subauroral Emission

The broad-scale structures of both dayside and nightside, shown in Figure 17 (top), are morphologically similar, as both are dominated by the main auroral emission (at 30°R$_J$, indicated by the vertical double lines). The nightside emission is far stronger at the poles, but this is likely to be a function of those regions with larger errors, both in the narrowness of the Jovimagnetic latitudes that contribute to it and the line-of-sight correction we have applied.

When the plot is scaled to 10% peak brightness, as shown in Figure 17 (middle), differences between the dayside and nightside emission become more apparent. Firstly, there is a significant difference in the equatorial emission on the dayside (solid black line) and nightside (dashed green line).

Rego et al. [2000] modeled the equatorial emission as resulting entirely from EUV ionization, shown by the dash-dotted red line, and this clearly provides the largest difference between the equatorial dayside and nightside emission. Secondly, the region in which the mid-to-low latitude emission exists on the dayside, modeled by the blue dash-triple dotted line, clearly has comparatively little counterpart emission on the nightside. In fact, taking into account the spatial resolution of the VIMS, the strong nightside H_3^+ emission is very close to the discrete auroral component with which *Rego et al.* [2000] models the main auroral emission (black dashed line). In the region within 10° of 5.9°R$_J$, there may be a significant component of mid-to-low latitude H_3^+ emission, though it is difficult to separate this emission from emission from the Io spot and trail. It is, however, notable that the CMLs used to observe by Rego, when compared with the SIII longitudes in Figure 11 are both longitudes where almost no subauroral emission is seen within the nightside emission.

In Figure 17 (bottom), we have replaced the nightside emission of the profile with one that averages over all Jovimagnetic longitudes, as discussed in section 3.4 and shown in Figure 9 (bottom). This has the combined effect of increasing the signal to noise of our observations and, at the same time, including a component of the brighter subauroral emission observed at longitudes away from those observed by *Rego et al.* [2000].

The longitudinally averaged emission appears to show more significant subauroral emission than the specific longitudes shown in the Rego study. The modeled mid-to-low latitude emission appears to match better with the decreasing nightside emission equatorward of 5.9°R$_J$. There remains a smaller but still significant difference between the dayside mid-to-low latitude emission and emission seen in the nightside.

6.3. Equatorial Emission

At latitudes equatorward of the region where *Rego et al.* [2000] notes significant mid-to-low latitude emission on the dayside, there is no evidence for any nightside emission in our data. It is possible that the nightside of Jupiter continues to decrease in temperature, so that any variation in the column density in this region would remain undetected due to the greatly reduced emission per molecule. However, the temperature of the dayside increases toward the equator [*Lam et al.*, 1997], a thermal structure that is likely to broadly rotate onto the nightside, and so it is reasonable to assume that the lack of any H_3^+ emission indicates the lack of any H_3^+ on the nightside equator at local times three hours either side of midnight (as shown in Figure 2). However, the lack of H_3^+ emission could be due to unexpectedly low equatorial temperature combined with the expected low column density.

Dayside H_3^+ ionization is driven by two significant processes at the equator: the ionization of H_2 by solar EUV, creating H_2^+, which in turn produces H_3^+, is almost instantaneous; and the ionization of H to create H^+, which then reacts with vibrationally excited H_2 ($v \geq 4$) to form H_2^+, in turn forming H_3^+, which occurs more slowly and thus delays the peak H_3^+ formation on the dayside by a few hours (H. Melin, private communication, 2015). Any dayside generated H_3^+ formed through EUV ionization will be lost on the nightside within ~15 min through recombination. As a result, the lack of any significant H_3^+ emission at the equator on the nightside is not unexpected, but it shows that while the reaction between H^+ and H_2 ($v \geq 4$) delays the production of H_3^+ because of the extended lifetime of H^+ in the upper atmosphere, the H^+ lifetime must be on the order of only a few hours, or this H^+ would still be producing equatorial H_3^+ well onto the nightside.

7. Discussion

Our observations of the nightside auroral emission provide the first-ever measure of the conditions in the nightside ionosphere of Jupiter. These allow us to understand how the ionosphere changes once the influence of the Sun has faded from view and, in turn, understand how the Sun affects the ionosphere. Our maps of emission, shown in section 4, clearly show the dominance of the aurora on the nightside ionosphere. Combined with the detailed comparison between day and nightside emissions in section 6, it shows that in equatorial regions close to midnight local time, the nonauroral nightside H_3^+ ionosphere effectively does not exist, as the dayside driven H_3^+ sources in this region have faded completely.

The morphology of mid-to-low latitude emission on the dayside of Jupiter has always been difficult to explain, but studies have focused on the possibility that the presence of H_3^+ in this latitude range is an indication of the precipitation of energetic particles from the inner magnetosphere or that this emission is driven by the thermal gradient away from the auroral region. Our observations of the nightside H_3^+ emission provide a new view on the subauroral region, allowing us to provide direct contrast with the dayside.

Closer to the auroral region, in subauroral regions located at latitudes that magnetically map between approximately 4 and 6 R_J, there is significant emission seen on the nightside, but this emission appears to be far more localized in longitude than on the dayside. Using measurements of temperature and column density from section 5, it appears that this emission is largely driven by changes in the localized density, with the drop off in temperature having a strong dampening effect on emission from lower latitudes. This asymmetric emission appears only loosely associated with potential regions of scattered particle precipitation in the north, while they do not match at all with these regions in the south. There is no evidence for scattered particle precipitation in the latitudes that map to 1.5 R_J from the planet, where the largest asymmetries in emission are expected, though this may in part result from the lower temperatures in this region.

This emission may alternatively result from subrotational winds transporting H^+ from the auroral regions zonally along lines of equal Jovigraphic latitude to regions where field lines map closer to the rotational pole, so that emission is observed at lower Jovimagnetic latitudes. However, the lack of any H_3^+ equatorial emission on the nightside that any H^+ created by solar EUV on the dayside is reduced after a ~3–9 h period to the point where no measurable H_3^+ is produced.

Differences observed between dayside and nightside emission in this subauroral region may result in local time differences in these processes. Certainly, the relative brightness of subauroral emission is far more

variable on the nightside than the dayside, as shown in Figure 11, and when localized nightside emission was averaged across all longitudes, day and nightside emission compared more favorably, as seen in Figure 17 (bottom). Additional differences between these profiles may be explained by the constant temperature used in *Rego et al.* [2000], where both dayside and nightside studies now show a decreasing temperature at subauroral regions [*Lam et al.*, 1997] (Figure 15). Indeed, a temperature gradient of only 300 K across the mid-to-low latitude emission region would explain all this emission, without the need for any source of additional H_3^+.

It is clear that the subauroral emission often described as "mid-to-low" latitude emission is actually far more complex than has previously been described. *Lam et al.* [1997] showed significant variability in both temperature and column density at both subauroral and nonauroral regions. Further investigation of both these regions on the dayside, where more emission is readily available, is obviously of great importance, as the observed variations could provide a key new diagnostic to magnetic models in a region where there are currently no limits.

Our observations also provide direct insights into the conditions within the planet's aurora. The similarity of the auroral region on both the dayside and nightside clearly shows that it is auroral processes that dominate in this region, with particle precipitation driving ionization and conductivity and with Joule heating driving the temperatures significantly higher than the surrounding subauroral regions.

Finally, these observations provide the first indicator for what the JIRAM instrument on Juno may observe on the nightside of Jupiter in 2016 and 2017. Using results from that mission, combined with new investigations of the dayside H_3^+ emission, we may at last understand how and to what extent energy deposited in the auroral region of the planet is dispersed through the entire upper atmosphere.

References

Abel, B., and R. M. Thorne (2003), Relativistic charged particle precipitation into Jupiter's sub-auroral atmosphere, *Icarus*, *166*, 311–319, doi:10.1016/j.icarus.2003.08.017.

Achilleos, N., S. Miller, J. Tennyson, A. D. Aylward, I. Mueller-Wodarg, and D. Rees (1998), JIM: A time-dependent, three-dimensional model of Jupiter's thermosphere and ionosphere, *J. Geophys. Res.*, *103*, 20,089–20,112, doi:10.1029/98JE00947.

Acton, C. H. (1996), Ancillary data services of NASA's Navigation and Ancillary Information Facility, *Planet. Space Sci.*, *44*, 65–70, doi:10.1016/0032-0633(95)00107-7.

Bhardwaj, A., and G. R. Gladstone (2000), Auroral emissions of the giant planets, *Rev. Geophys.*, *38*, 295–354, doi:10.1029/1998RG000046.

Brown, R. H., et al. (2003), Observations with the Visual and Infrared Mapping Spectrometer (VIMS) during Cassini's flyby of Jupiter, *Icarus*, *164*, 461–470, doi:10.1016/S0019-1035(03)00134-9.

Connerney, J. E. P., M. H. Acuna, N. F. Ness, and T. Satoh (1998), New models of Jupiter's magnetic field constrained by the Io flux tube footprint, *J. Geophys. Res.*, *103*, 11,929–11,940, doi:10.1029/97JA03726.

Cowley, S. W. H., and E. J. Bunce (2001), Origin of the main auroral oval in Jupiter's coupled magnetosphere-ionosphere system, *Planet. Space Sci.*, *49*, 1067–1088, doi:10.1016/S0032-0633(00)00167-7.

Drossart, P., et al. (1989), Detection of H_3^+ on Jupiter, *Nature*, *340*, 539–541, doi:10.1038/340539a0.

Feldman, P. D., M. A. McGrath, H. W. Moos, S. T. Durrance, D. F. Strobel, and A. F. Davidsen (1993), The spectrum of the Jovian dayglow observed at 3 Å resolution with the Hopkins ultraviolet telescope, *Astrophys. J.*, *406*, 279–284, doi:10.1086/172439.

Gladstone, G. R., J. H. Waite, and W. S. Lewis (1998), Secular and local time dependence of Jovian X ray emissions, *J. Geophys. Res.*, *103*, 20,083–20,088, doi:10.1029/98JE00737.

Gladstone, G. R., et al. (2007), Jupiter's Nightside Airglow and Aurora, *Science*, *318*, 229–231, doi:10.1126/science.1147613.

Grodent, D., J. T. Clarke, J. Kim, J. H. Waite, and S. W. H. Cowley (2003a), Cowley Jupiter's main auroral oval observed with HST-STIS, *J. Geophys. Res.*, *108*(A11), 1389, doi:10.1029/2003JA009921.

Grodent, D., J. T. Clarke, J. H. Waite, S. W. H. Cowley, J.-C. Gérard, and J. Kim (2003b), Jupiter's polar auroral emissions, *J. Geophys. Res. 108*(A10), 1366, doi:10.1029/2003JA010017.

Grodent, D., B. Bonfond, J.-C. GéRard, A. Radioti, J. Gustin, J. T. Clarke, J. Nichols, and J. E. P. Connerney (2008), Auroral evidence of a localized magnetic anomaly in Jupiter's northern hemisphere, *J. Geophys. Res.*, *113*, A09201, doi:10.1029/2008JA013185.

Hess, S. L. G., B. Bonfond, P. Zarka, and D. Grodent (2011), Model of the Jovian magnetic field topology constrained by the Io auroral emissions, *J. Geophys. Res.*, *116*, A05217, doi:10.1029/2010JA016262.

Lam, H. A., N. Achilleos, S. Miller, J. Tennyson, L. M. Trafton, T. R. Geballe, and G. E. Ballester (1997), A baseline spectroscopic study of the infrared auroras of Jupiter, *Icarus*, *127*, 379–393, doi:10.1006/icar.1997.5698.

Lystrup, M. B., S. Miller, N. Dello Russo, R. J. Vervack Jr., and T. Stallard (2008), First vertical ion density profile in Jupiter's auroral atmosphere: Direct observations using the Keck II telescope, *Astrophys. J.*, *677*, 790–797, doi:10.1086/529509.

Melin, H., S. Miller, T. Stallard, C. Smith, and D. Grodent (2006), Estimated energy balance in the Jovian upper atmosphere during an auroral heating event, *Icarus*, *181*, 256–265, doi:10.1016/j.icarus.2005.11.004.

Melin, H., T. S. Stallard, J. O'Donoghue, S. V. Badman, S. Miller, and J. S. D. Blake (2014), On the anticorrelation between H_3^+ temperature and density in giant planet ionospheres, *Mon. Not. R. Astron. Soc.*, *438*, 1611–1617, doi:10.1093/mnras/stt2299.

Miller, S., R. D. Joseph, and J. Tennyson (1990), Infrared emissions of H3(+) in the atmosphere of Jupiter in the 2.1 and 4.0 micron region, *ApJ Lett.*, *360*, L55–L58, doi:10.1086/185811.

Miller, S., N. Achilleos, G. E. Ballester, H. A. Lam, J. Tennyson, T. R. Geballe, and L. M. Trafton (1997), Mid-to-low latitude H_3^+ emission from Jupiter, *Icarus*, *130*, 57–67, doi:10.1006/icar.1997.5813.

Miller, S., et al. (2006), H_3^+: The driver of giant planet atmospheres, *Philos. Trans. A Math. Phys. Eng. Sci.*, *364*, 3121–3137, doi:10.1098/rsta.2006.1877.

Miller, S., T. Stallard, H. Melin, and J. Tennyson (2010), H_3^+ cooling in planetary atmospheres, *Faraday Discuss.*, *147*, 283, doi:10.1039/c004152c.

Miller, S., T. Stallard, J. Tennyson, and H. Melin (2013), Cooling by H_3^+ emission, *J. Phys. Chem. A*, *117*, 9770–9777, doi:10.1021/jp312468b.

Morioka, A., S. Yaegashi, H. Nozawa, H. Misawa, Y. S. Miyoshi, F. Tsuchiya, and S. Okano (2004), H_3^+ emissions in the Jovian sub-auroral region and auroral activity, *Geophys. Res. Lett.*, *31*, L16806, doi:10.1029/2004GL020390.

Neale, L., S. Miller, and J. Tennyson (1996), Spectroscopic properties of the H_3^+ H_3^+ molecule: A new calculated line list, *Astrophys. J.*, *464*, 516, doi:10.1086/177341.

Radioti, A., M. Lystrup, B. Bonfond, D. Grodent, and J.-C. Gérard (2013), Jupiter's aurora in ultraviolet and infrared: Simultaneous observations with the Hubble Space Telescope and the NASA Infrared Telescope Facility, *J. Geophys. Res. Space Physics*, *118*, 2286–2295, doi:10.1002/jgra.50245.

Raynaud, E., E. Lellouch, J.-P. Maillard, G. R. Gladstone, J. H. Waite, B. Bézard, P. Drossart, and T. Fouchet (2004), Spectro-imaging observations of Jupiter's 2-μm auroral emission. I. H_3^+ distribution and temperature, *Icarus*, *171*, 133–152, doi:10.1016/j.icarus.2004.04.020.

Rego, D., N. Achilleos, T. Stallard, S. Miller, R. Prangé, M. Dougherty, and R. D. Joseph (1999), Supersonic winds in Jupiter's aurorae, *Nature*, *399*, 121–124, doi:10.1038/20121.

Rego, D., S. Miller, N. Achilleos, R. Prangé, and R. D. Joseph (2000), Latitudinal profiles of the Jovian IR emissions of H_3^+ at 4 μm with the NASA Infrared Telescope Facility: Energy inputs and thermal balance, *Icarus*, *147*, 366–385, doi:10.1006/icar.2000.6444.

Stallard, T., S. Miller, G. Millward, and R. D. Joseph (2001), On the dynamics of the Jovian ionosphere and thermosphere: I. The measurement of ion winds, *Icarus*, *154*, 475–491, doi:10.1006/icar.2001.6681.

Stallard, T., S. Miller, G. Millward, and R. D. Joseph (2002), On the dynamics of the Jovian ionosphere and thermosphere: II. The measurement of H_3^+ vibrational temperature, column density, and total emission, *Icarus*, *156*, 498–514, doi:10.1006/icar.2001.6793.

Stallard, T., et al. (2008), Complex structure within Saturn's infrared aurora, *Nature*, *456*, 214–217, doi:10.1038/nature07440.

Stallard, T. S., S. Miller, S. W. H. Cowley, and E. J. Bunce (2003), Jupiter's polar ionospheric flows: Measured intensity and velocity variations poleward of the main auroral oval, *Geophys. Res. Lett.*, *30*(5), 1221, doi:10.1029/2002GL016031.

Tao, C., S. V. Badman, and M. Fujimoto (2011), UV and IR auroral emission model for the outer planets: Jupiter and Saturn comparison, *Icarus*, *213*, 581–592, doi:10.1016/j.icarus.2011.04.001.

Vasavada, A. R., A. H. Bouchez, and A. P. Ingersoll (1999), Jupiter's visible aurora and Io footprint, *J. Geophys. Res.*, *104*, 27,133–27,142, doi:10.1029/1999JE001055.

Waite, J. H., G. R. Gladstone, W. S. Lewis, P. Drossart, T. E. Cravens, A. N. Maurellis, B. H. Mauk, and S. Miller (1997), Equatorial X-ray emissions: Implications for Jupiter's high exospheric temperatures, *Science*, *276*, 104–108, doi:10.1126/science.276.5309.104.

Yelle, R. V., and S. Miller (2004), Jupiter's thermosphere and ionosphere, in *Jupiter: The Planet, Satellites and Magnetosphere*, pp. 185–218, Cambridge Univ. Press, Cambridge, U. K.